Erasmus+

COSI Computational Colour and Spectral Imaging

Master in Computational Colour and Spectral Imaging (COSI)

UNIVERSITY OF EASTERN FINLAND · UNIVERSIDAD DE GRANADA · UNIVERSITÉ DE LYON · UNIVERSITÉ JEAN MONNET SAINT-ÉTIENNE · NTNU Norwegian University of Science and Technology

Optical Design of a Human Eye Inspired Lens

Master Thesis Report

Presented by

Fernando Linares Quirós

and defended at the

Norwegian University of Science and Technology

September 2023

Academic Supervisor(s): Docent, Pauli Fält, PhD
Host Supervisor: Prof. Simon Thibault, PhD, Eng.
Jury Committee:

1. Prof. Ivar Farup, NTNU, Norway
2. Prof. Luis Gómez Robledo, UGR, Spain

Submission of the thesis: 10th August 2023
Day of the oral defense: 4th September 2023

Abstract

Nature provides one of the most complex and stunning imaging devices found nowadays. The human eye has been studied over centuries and the research community is still trying to totally understand it. With the main interest put in the medical field, numerous anatomical models have been proposed trying to replicate this human organ and psychophysical models to understand the image processing carried out inside the brain. In this thesis, another attempt to understand this device is conducted with the aim to replicate as closely as possible the imaging capabilities of the eye while respecting its form-factor characteristics. To develop the design, the use of the optical modelling software CODE V is used, where the different eye constraints are established. Using as a starting point a monochromatic spherical design, six different setups are proposed, showing that the number of optical surfaces employed can be considerably reduced by using aspherical/conic surfaces. The implementation of an achromatic doublet will also increase the performance considerably. The implementation of a curved sensor mimicking the retina does not improve significantly the results obtained and there is a trade-off between imaging capabilities and optical aberrations.

Acknowledgment

I want to thank my brother, for being my main support in life and for keeping me going through these months. I would also like to thank my friends and family, especially Mar, for being always there supporting me. Also refer to all the wonderful people that I met during this period in Canada, that made this work more bearable and joyful.

I would also like to deeply thank Guillaume Allain, for his daily support, advice and supervision throughout the whole internship. I would also like to thank my supervisors Simon Thibault and Pauli Fält for their useful advice and guidance during this period.

Acronyms

AR	Augmented reality
AUT	Automatic design
AX	Axial color
CAGE	Chromatic aspherical gullstrand exact
CCD	Charge-couple device
CIE	Commission Internationale de l'Éclairage
CMOS	Complementary Metal-Oxide-Semiconductor
cpd	cycles per degree
CS	Contrast sensitivity
CSF	Contrast sensitivity function
DoF	Depth of field
DST	Distortion
EFL	Effective focal length
FoV	Field of view
FPA	Focal plane array
HS	Hartmann-Shack
HVS	Human visual system
IOL	Intraocular lens
LAT	Lateral color
LSF	Line spread function
MTF	Modulation transfer function
NA	Numerical aperture
OAL	Overall length
PMMA	Polymethyl Methacrylate
PRK	Photorefractive Keratectomy
PSF	Point spread function
PTB	Petzval blur
PTZ	Petzval/Field curvature
RI	Relative illumination
SA	Spherical aberration
SAS	Sagittal astigmatism
TAS	Tangential astigmatism
TCO	Tangential coma
VR	Virtual reality

Contents

1 Introduction

The human eye is one of the most complex imaging systems available. Its anatomical and physiological properties have always been under evaluation and human vision theories are constantly modified and updated in order to accurately understand how our vision works and which physical/chemical processes take place on them. The visual stimulus has to reach the retina, going through all the optical components (cornea, aqueous humour, lens and vitreous humour) and once here, it is transformed into a neural response to reach the brain cortex (occipital lobe). The eye can be considered as an instrument able to detect stimuli and image them, where the retina acts as a high-resolution photosensor capable of differentiate colors. When both eyes work together, they provide binocular vision that allows one to determine the location, distance, depth and speed of distant objects in three dimensions. The eye's structure and the performance between the muscles, brain and nerves create rapid feedback for a constant accommodation and ocular movement, in order to provide optimal vision.

One of the main reasons that motivate us to study these properties relies on the medical field. The necessity to assess eye diseases (cataracts, diabetic retinopathy, glaucoma, age-related macula degeneration, etc.) or refractive errors (refractive surgery, photorefractive keratectomy, intraocular lens implantation) needs first a full comprehension and study of how this 'imaging device' works. It is for this reason that the scientific community have tried, not only to understand the properties of the eye but also to reproduce them from an anatomical and physiological point of view, trying to resemble as close as possible to them, in order to test novel techniques or treatments Gobbi et al. (1999); Curatu et al. (2002); Norrby et al. (2007); Atchison et al. (2008).

In this thesis, a new approach will be presented trying to merge a schematic optical model layout while respecting the imaging performance of the human eye. This is done in order to mimic the form factor and reproduce the imaging requirements of the eye. A neurophysical model is also included in order to evaluate the noise generated internally in the eye, accounting for the human signal processing of the image Gobbi (2012). This work is a continuation of the research developed by Allain and Thibault (2022), which will be used as a starting reference point as well as

a comparison for the proposed designs. This starting setup was monochromatically improved, considerably reducing the number of surfaces required. Polychromatic layouts have been also proposed, presenting a gradual increase of the imaging performance while also trying to meet the rest of the constraints. The use of a curved sensor is also considered but no significant improvements were reached under this architecture. With this combined model, the perceptive and optical properties of the model eye will be evaluated. In other words, the imaging capabilities are assessed by looking at the modulation transfer function (MTF) and contrast (C_{thresh}) achieved in the system. All of these models have been prototyped with the optical software CODE V Synopsys, Inc. (2023).

The content of this thesis is organized as follows: In Chapter 1, the main research topic under study is presented, as well as the challenge and tasks that will be attempted to solve. Also, a brief background study is presented in order to help the reader to understand better some concepts. This is followed by a review of the different research groups that have attempted similar procedures or challenges and state of the art. In Chapter 2 the methodology is presented, with the different tools and procedures followed in order to solve the problem. The constraints required to build the model are presented, as well as the software used, CODE V Synopsys, Inc. (2023) and the pipeline followed in it. In Chapter 3 the experiments done and the results achieved are presented with their corresponding discussion. To sum up, the conclusion is presented in Chapter 4.

AI software tool Chat GPT OpenAI (2021) was used for the visualization code in Overleaf while structuring tables or figures. No AI tool has been used to write this report, just used Word Reference to verify some meanings and apply different synonyms.

1.1 Background study

1.1.1 Contrast Sensitivity Function

One reliable and accurate way to evaluate an optical system is through contrast sensitivity (CS). This basically provides us with information if the system is able to resolve the contrast between two areas with different luminosity or not. CS is the minimum contrast threshold required for a certain detection probability. This contrast information can be gathered in contrast sensitivity function (CSF) which provides a visual representation of the sensitivity of a system capable to resolve (or not) narrow-banded stimulus (spatial frequency) Dartt (2010) Hou et al. (2021) Roka et al. (2009).

In Fig. 1.1, an example of a contrast sensitivity function is shown. Note that

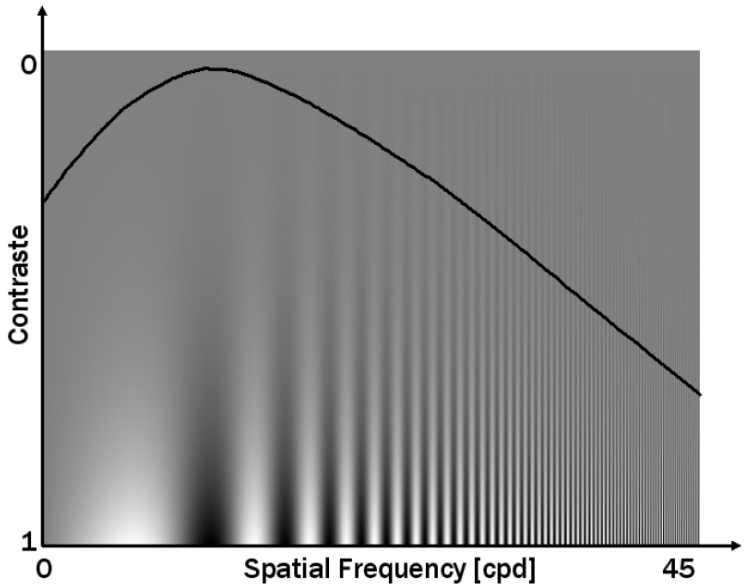

Figure 1.1: *Example of a certain contrast sensitivity function(CSF) for the human eye. The plot represents the contrast perceived (0 to 1) vs the spatial frequency in cycles per degree (cpd). The visual example of black/white grids is also depicted. The figure is taken from Hautière et al. (2007).*

this curve is obtained for certain stimuli, under certain conditions (luminosity, pupil size, subject, etc.). CSF is usually measured in cycles per degree (cpd) or in cycles per mm, where a cycle accounts for a black/white grid. A visual example of black/white grids is also provided in Fig. 1.1. CSF is very useful in the human eye domain since it reflects both the effect of the optical part and the neural processing part of our visual system. Several CSF models for the human eye have been proposed throughout the years, where the main problem is the huge inter-individual variability between subjects and stimulus. Providing a general CSF accounting for all the population is quite a challenge since it is typically measured using psychophysical techniques. Several approaches will be reviewed in section 1.2.2.

1.1.2 Modulation Transfer Function

Another useful concept required for a good evaluation of imaging systems is the modulation transfer function (MTF), which tells us the capability of the imaging system to transfer as close as possible the spatial frequencies of the object to the image. MTF is usually measured by imaging a series of sine-wave patterns of

different spatial frequencies and calculating the ratio of the contrast of the pattern in the image to the contrast of the pattern in the object Ahmed (2007). This is usually performed using a Line Spread Function (LSF) (see Imatest (2023) and iso 16505 eSFR)

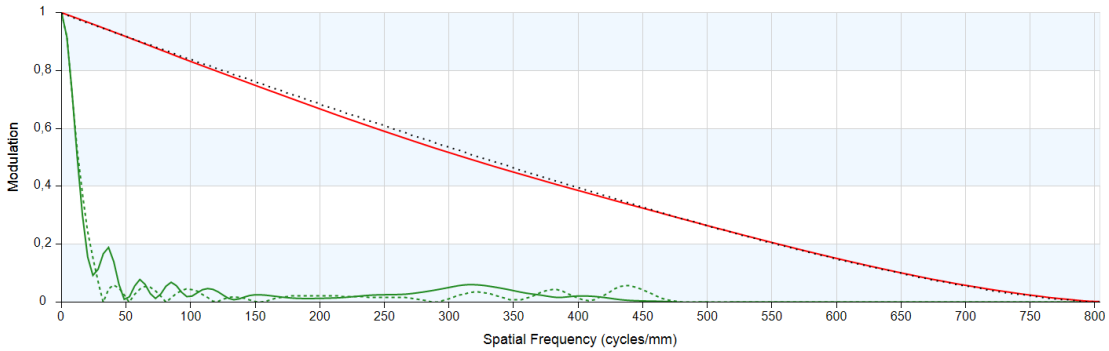

Figure 1.2: *Example of a certain Modulation Transfer Function (MTF) for an optical design. This graph represents the modulation (from 0 to 1) vs the spatial frequency in cycles per mm. Two different MTFs are plotted. The red line corresponds to the MTF obtained for the central field (0 degrees decenter) and two green lines correspond to the 80 degree field. The continuous line corresponds to the tangential rays and the dashed line corresponds to the sagittal rays. The image is obtained from the optical software CODE V Synopsys, Inc. (2023).*

In Fig. 1.2, an example of a modulation transfer function is shown, obtained from an optical design in CODE V. It is an optical design software designed by Synopsys, Inc. Synopsys, Inc. (2023). It is mostly used to design optical or illumination systems. CODE V will be later explained in Chapter 2. The MTF is usually expressed in cycles/mm or cycles/degree. As depicted in Fig. 1.2, there are two curves, one red referring to a central field resolution and one green referring to 80 degrees peripheral field resolution. This certain degree refers to the resolution obtained on axis with the system (central) and another measurement taken from a field 80 degrees off-axis. Both concepts MTF and CSF are closely related, but they represent different aspects. They are both metrics used in optics and vision science to characterize the performance of imaging systems and human visual perception and they work in the spatial frequency domain. But MTF provides information about the system transferring spatial frequencies from the object to the image, whereas CSF tells us if the visual system is capable to distinguish in contrast/luminance certain stimuli in different spatial frequency ranges. To sum up, it can be stated that MTF measures the imaging system's ability to transfer spatial frequencies whereas CSF measures the visual system's ability to detect contrast at different spatial frequencies.

1.1.3 Human's eye optical path

In this section, a brief summary of the eye's optical pathway is provided in order to get a better understanding of some concepts later developed and the project itself. Two main parts can be separated when discussing the eye's pathway. The first one is the optical path, where the signal is still a light stimulus (photons) and goes through all the optical surfaces of the eye to reach the retina (See Fig. 1.3). The second path is called the neural path, and it starts when the light stimulus is converted to an electric response in the retina and is transferred as nerve impulses to the optic nerve. The neural path finishes when those impulses reach the brain cortex.

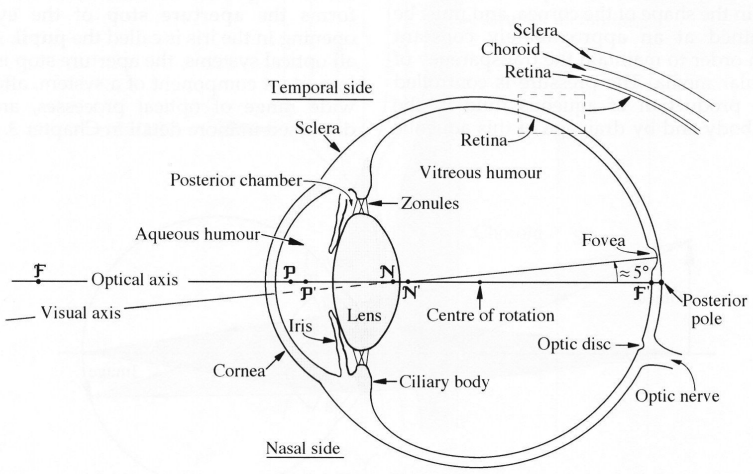

Figure 1.3: *Scheme of a human eye describing all the optical surfaces up to the retina. The image is taken from Atchison (2023).*

The optical path starts right away in the cornea, the first surface that the light reaches. Most of the optical power in the eye is provided by this surface (around 43 diopters) that is approximately 0.55 mm thick and has an average radius of curvature of 7.7 mm Atchison (2023). It is expressed as an average radius since the cornea has an aspherical surface, which means that the radius is not constant throughout the whole surface. The cornea has an average aspheric parameter of $K = -0.28$, which means that it has an ellipsoid shape. The second area along the optical path would be the aqueous humour (refractive index of 1.336 for a central wavelength of 587.6 nm), followed by the iris which is another crucial part of the eye, responsible for regulating the amount of light entering the eye. The pupil's diameter ranges from 1.5 - 2 mm under bright light conditions and up to 7 - 8 mm for dark environments Atchison (2023). This diameter range is narrowed with age Charman and Radhakrishnan (2009). Note that for large pupil

diameters, relatively strong optical aberrations will be present, and for small pupil diameters, diffraction will affect the image formation on the retina, so the iris clearly determines a good part of the image quality. After the iris follows the lens, which provides the rest of the optical power in the eye. The lens is also mainly responsible for the eye's accommodation process in order to constantly focus on the observed stimulus. It is a biconvex lens where two main parts can be differentiated: the outer part (or the cortex), and the inner part (or the nucleus). The lens never stops growing throughout life, adding several layers, thus increasing its thickness Cook et al. (1994). There is no exact measure of its refractive index distribution. The lens of the eye is one of the most challenging optical components to replicate since the fluctuation of its parameters (thickness, refractive index) depending on the focus point are constantly changing. It is also heavily influenced by factors like age (opacification). Along the optical path, the lens is followed by vitreous humour. Finally, the stimulus reaches the retina, where the light is collected by photoreceptors. Atchison (2023). Specifically, light is focused on the fovea, the area of sharp central vision in the retina. Here the first optical path ends, and several theoretical eye models have been developed to replicate it, such as the widely known Gullstrand eye model Gullstrand (1909).

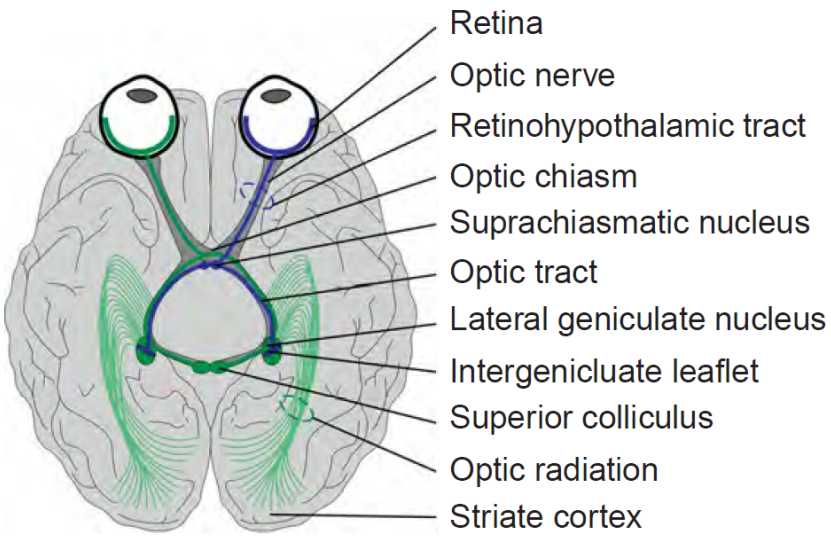

Figure 1.4: *Neural path of the eye. Starting in the retina and finishing in the occipital lobe of the brain. The figure is taken from Dartt (2010).*

A schematic example of the human eye can be observed in Fig. 1.3, where the different parts of the human eye are represented. It can also be observed that the optical axis of the eye is different to the visual one. The optical axis represents exactly the straight line entering from the middle of the cornea up to the retina.

The visual axis represents the 5 degrees tilted line where vision points, since the fovea is located 5° temporally, as depicted in Fig. 1.3. In the different theoretical eye models, this 5° tilt present for the fovea is neglected. In Fig. 1.3 are also represented the different cardinal points: focal points (F and F'), principal points (P and P'), nodal points (N and N').

In the retina starts the neural path, when the light gets converted in the photoreceptors into neural activity Eglen (2012). There are two different types of photoreceptors: cones and rods. The cones mainly work under photopic conditions (high luminosity such as bright daylight, office work, etc). There are three different types of cones, each of them sensitive to a certain wavelength: L-cones sensitive to long wavelength range, M-cones sensitive to middle wavelength range and S-cones sensitive to short wavelength range. As a combination of these three types of cones, colour is perceived. The rods are responsible for scotopic vision. This concept accounts for low luminosity conditions, which mainly occur during the night. This type of photoreceptor gets saturated at high luminosity levels. Since there is only one type of rod, no colour discrimination is possible in low-light conditions. The state between photopic and scotopic conditions is called mesopic, and it happens when rods and cones contribute to visual perception. This happens when the light conditions are not too bright, nor too dark. The spatial distribution of the cone and rod photoreceptors in the retina is called an eye mosaic. This is one of the key factors to understand in order to provide a good eye model since photoreceptors density decreases the further we move from the retinal area of sharp central vision (macula and fovea). Visual acuity decreases the further the stimulus gets from the fovea. That is why eye contrast models usually also take into account this eccentricity. This phenomenon basically tells the distance between a stimulus perceived and the fovea (central retina). If a stimulus is observed straight ahead, the fovea is aligned with the center of the pupil and the eccentricity would be zero. It has been proved that a task is performed better if it is presented close or in the fovea Staugaard et al. (2016). Consequently, the detection time and error rates will increase the further the stimulus moves from the macula/fovea Staugaard et al. (2016). Once the neural response (signal) is transmitted through and processed by the retinal cells (i.e., horizontal, bipolar, amacrine and ganglion cells), the signal continues to the brain via optic nerve fibres thus merging into the optic nerve. This neural path goes through the brain passing through the optic chiasm, optic tract, lateral geniculate nucleus of the thalamus and finally projected through optic radiations to the visual cortex located in the occipital lobe. The neural pathway and its different parts are depicted in Fig. 1.4. Note that this neural process is extremely complex, and is considerably simplified in this section. The scientific community has investigated for a long time and still investigating how this neural pathway transfers visual information. Many attempts to mimic the effect of this

neural effect have been done in the different contrast sensitivity functions (CSFs) proposed over the years. A detailed description of the optical and neural pathway can be found in Dartt (2010); Atchison (2023).

1.2 Literature review

This section will review theoretical eye models, some of the most relevant CSFs developed for the human eye, as well as some other optomechanical eye models for different purposes.

1.2.1 Theoretical eye models

Theoretical eye models have been developed in order to reproduce anatomic parameters of the eye (cornea, iris, lens, retina). It is difficult to state who developed the very first eye model, since humans have been always studying how our visual system works in order to understand it better. Contributions throughout the years by many scientists such as Kepler Jaeger (1986), Descartes and Scheiner were crucial for the better understanding of the human eye. The first important hint regarding eye models was made by Huygens. He constructed a tangible eye model that consisted of two hemispheres filled with water and a diaphragm. However, it was not until the early 1800s when Thomas Young created the initial description of the cornea and lens in geometric optics. Young was able to estimate the radii of curvature for these surfaces, along with the anterior chamber length and the different refractive index values, which were impressively accurate for the time period. Continuous improvements have been made afterwards by Moser, Listing, Helmholtz or Tscherning, by specifying more accurately radius of curvature, surface thickness, etc Artal and Tabernero (2010); Atchison (2023); Atchison and Thibos (2016).

It could be established as an important moment for these theoretical eye models when the well-known Gullstrand Eye model was published in 1909 Gullstrand (1909). The Gullstrand eye model consists of six spherical surfaces. Two of them account for the anterior and posterior surfaces of the cornea and four other surfaces account for the lens. Additionally, the Gullstrand model included two sets of parameters: one for the relaxed-eye condition and another for the accommodating condition, which used a lens with higher refractive power. There is also a reduced version of this model, where the cornea is treated as a single refractive surface. Despite the fact that this model does not account for optical aberrations, it is still used in many studies and optometry handbooks since it was the first model developed that was anatomically accurate.

With the continuous improvement of technologies, and by measuring accurately in vivo the different surfaces of the eye, these models have been refined, providing a more accurate insight, in many different ways. This refining has been done, for example, by adding non-spherical (aspherical) surfaces, shell structure or a gradient refractive index (GRIN) in order to mimic the lens. This kind of GRIN lens, instead of adding abruptly the desired refractive index right after the surface like a traditional model, is added gradually, as its name specifies. Then, the refractive index will change throughout the whole volume of the lens. The very first concept of this gradient index lens started with the Gullstrand eye model Gullstrand (1909), where the lens is divided in two areas with different refractive indices, as a shell structure. Other studies have been devoted to understand accurately this shell representation of the lens Masajada (1999) and many other authors since then Pomerantzeff (1971); Al-Ahdali and El-Messiery (1995); Liu et al. (2005) have been mimicking this shell with numerous layers (300 and up to 602 refractive index shell layers). Mathematical expressions have been also proposed accounting for gradient index models, such as the ones in Liou and Brennan (1997). The changes in the lens and the rest of the surfaces in the eye have also been modelled for different age groups since it is known that they vary depending on the age, such as the Arizona model Greivenkamp et al. (1995).

Here are listed some of the main models chronologically developed with their principal characteristics:

- *Emsley* Emsley (1936). With a single spherical surface proposed, the aberration and image formation relies only on it, with a refractive index of 1.333, resembling water. It provides a fast overview of the eye, for an introductory understanding.

- *Kooijman* Kooijman (1983). Kooijman developed an eye model that included both spherical and aspheric surfaces with the purpose to calculate the distribution of retinal illumination for a Ganzfeld luminance field. The resulting distribution was found to be nearly uniform across the entire retina, and this homogeneity was not affected significantly by the pupil size or any other optical surfaces. Kooijman also determined the retinal area and luminous flux entering the eye as a function of the visual field size and described the length of the light path through the crystalline lens and the angle of incidence on the retina as functions of the visual field angle. This model was useful for the evaluation of the light distribution throughout the eye retina mosaic.

- *Thibos* Thibos et al. (1992). Another reduced eye model is proposed here, with a more accurate approach since they try to vary the refractive index of the model according to the wavelength evaluated, in order to provide a better

evaluation of chromatic aberrations. The spherical surface in Emsley (1936), is replaced with an aspherical one, in order to reduce spherical aberrations.

- *Arizona* Greivenkamp et al. (1995). This exact eye model tries to predict changes in the different surfaces of the eye related to the age, according to anatomical data. Several formulas are provided, to calculate thickness, radius, conic parameter and refractive index depending on the age. Although it does not propose a gradient index model to mimic the lens, the aberrations can be more or less predicted by playing with its dispersion and conic constant.

- *Liou and Brennan* Liou and Brennan (1997). Liou and Brennan model consists of four aspheric refracting surfaces, where the lens is evaluated under a gradient index model. It was developed to evaluate human vision under surgical procedures, contact lenses and spectacle lenses. Spherical and chromatic aberrations are estimated precisely with this model. It also provides good biometric data for the different refracting surfaces since it makes a comparison of the data gathered by different researchers.

- *Navarro* Escudero-Sanz and Navarro (1999). Several eye models have been proposed by this author. The first one was only devoted to reproduce images on axis, and then extended to a wide-angle model to evaluate retina images adding a spherical surface. An example of an exact eye model, consisting of four conic surfaces and lastly a spherical one for image formation. Aberrations, spot diagrams and MTF are evaluated for this eye model, accounting for a field degree of 120° (human eye FoV is 160°).

This is just a brief summary of the different eye models proposed, each of them mainly created for certain reason (image size evaluation, quantify aberrations, effects of human view with lenses, etc.). Depending on their complexity or number of surfaces, four different classification groups for these models can be established:

- *Reduced eye models.* These kinds of eye models are the simplest ones since they account for only one refracting surface. They are anatomically inaccurate but are useful to provide an approximate position of the cardinal points of the eye and the retinal image size. They are also a useful tool for students starting to get used to eye models, due to their simplicity Atchison and Thibos (2016); Gobbi (2012). Emsley eye model is a clear example Emsley (1936), shown in Fig. 1.5A, or Thibos eye model Thibos et al. (1992).

- *Simplified eye models.* They are still anatomically inaccurate but account for a larger number of surfaces, three in total. One surface accounting for the cornea and two for the lens. The aperture stop is placed correctly in

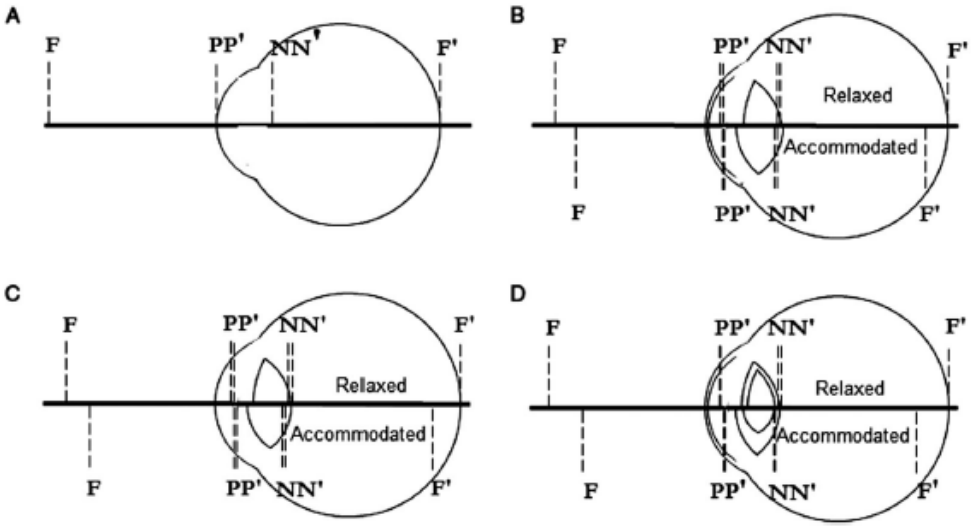

Figure 1.5: *Comparison of four different schematic eye models. 5.A corresponds to the Emsley reduced eye model. 5.B is the Gullstrand-Emsley simplified eye. 5.C Le Grand simplified eye. 5.D Gullstrand number one exact eye model. Note that for B, C and D the relaxed version of the model is provided in the upper part whereas the accommodated version is provided in the lower part. Their corresponding cardinal points are also depicted. The figure is taken from Atchison and Thibos (2016).*

those models. These kinds of models are often more favourable for calculating refractive error and accommodation because using more complex models may not result in significant improvements in accuracy. An example for this category is provided by the Gullstrand-Emsley modified eye model Emsley (1936) shown in Fig. 1.5B, or Le Grand simplified depicted in Fig. 1.5C.

- *Exact eye models.* At least one more refractive surface is added in these kinds of models (four or more in total). Two accounting for the cornea and two or more for the lens, usually to reproduce the gradual refractive index present in the lens. Several exact models are proposed, accounting for relaxed or accommodated versions of the lens. An example is the Gullstrand eye model number one "exact" Gullstrand (1909), as shown in Fig. 1.5D. They are useful for paraxial evaluation, refractive errors or reflections produced by the different surfaces.

- *Finite eye models.* This group accounts for more refined models, accounting for wide angle models, gradient index or shell models and exact tilt or decenters of the anatomical surfaces. In order to obtain a deeper evaluation of the eye

properties such as first and third-order aberrations, retinal image size, image quality, illumination, peripheral vision, etc. An example would be the eye model proposed by Liou and Brennan, with the gradient index lens model Liou and Brennan (1997). The eye prototype proposed in this thesis would also fall under this category.

In Fig. 1.5 are represented four different schematic eye models in order to get a better visual representation of these different models. One reduced model, one simplified and two exact eye models are presented.

After reviewing the different parameters proposed by the different eye models, only slight differences are observed and they do not lead to big discrepancies between them. More differences arise when evaluating and comparing image quality metrics or aberrations Gobbi (2012).

1.2.2 Contrast Sensitivity Function models for Human Vision

Reproducing the eye only from an anatomical point of view is not enough to simulate the visual path. One of the most difficult traits to mimic is the image processing pipeline of our visual system since many factors modify this image perception and the theories about how vision works are constantly evolving. This can be evaluated through the contrast sensitivity function (CSF). Contrary to the parameters such as the colorimetric functions where a standard has been established CIE (1931), unfortunately, there is no such standardization for the CSF. Even though this contrast sensitivity behaviour has been studied for several decades, only some models have been proposed Rovamo et al. (1993); Movshon and Kiorpes (1988); Thomas et al. (1993); Daly (1992). The Barten model Barten (1999) is one of the most well-known models, since it takes into account most of the factors influencing their fluctuations (photoreceptor densities, psychometric function, spatial and temporal frequencies of the luminance, neural noise, etc.) and provides useful mathematical equations that are quite easy to apply and useful in this kind of application. Since the release of these models in the late 20th century, very few new independent models have been published. This may be caused by the fact that gathering enough data from different subjects is a time-consuming task. Researchers usually use and compare different datasets from other studies in order to save a considerable amount of time. Some authors have tried to correct or modify this Barten's model since it makes some assumptions or sometimes lacks from theoretical support in several aspects. In Westland et al. (2006), a slight modification of Barten's model is introduced, where they wanted to include the chromatic effect present in the eye on the CSF since the original Barten model only

takes into account achromatic stimuli. Modifications related to Barten's peripheral vision are introduced in Bozorgian et al. (2022), by modifying the Neural noise term and Optical MTF, considerable differences are achieved the more eccentricity available. Note that the neural noise term accounts for the noise induced in the image quality by the brain processing (neural pathway) and the optical MTF is the image quality achieved in the eye after passing through every optical surface, without taking into account the neural pathway. A slightly different approach is proposed in Roka et al. (2009), where, instead of dividing the contrast sensitivity into Optical MTF and Neural MTF blocks (image quality after the optical pathway and the neural pathway), they state two new block concepts: Low pass MTF and High pass MTF, without considering if this noise originates from the neural/optical part Roka et al. (2009). According to Roka et al. (2009), the low pass components of the human CSF come from: optical aberrations (astigmatism, coma, defocus, etc.), stray light and scattering throughout the ocular media, diffusion in the retina, structure of the cones and the low pass component of the bandpass filtering of the neural processing in the retina. Whereas the high pass components are: The neural-based bandpass filtering, which involves lateral inhibition and the concentric receptive fields of midget ganglion cells. Their proposed algorithm vs Barten one is depicted in Fig. 1.6, with the division into different blocks for a better understanding of it. The formulae provided in this model are straightforward and state to provide a better fitting than the previous models since it gives higher accuracy and also a theoretical background for some aspects that were not covered in Barten's model.

The latest and most promising model developed is the so-called stelaCSF Mantiuk et al. (2022). This model has been developed after evaluating 11 different datasets, and then a general evaluation metric is proposed, so this will provide a more general approach and hopefully a better evaluation of the CSF, since it takes into account the most relevant dimensions of the stimulus (spatial and temporal frequency, eccentricity, luminance, and area). This model is focused on augmented reality (AR) and virtual reality (VR) applications since it can assess spatiotemporal deficiencies in an efficient way.

It is important to highlight the importance of the first proposed CSF metrics (Barten Barten (1999), Rovamo Rovamo et al. (1993), etc.) since all of the new ones either rely on or make assumptions based on these models. It would be also interesting to collect new and updated datasets regarding psychophysical experiments, since even the latest metrics developed, mostly rely on datasets published on the second half of the 20th century. Many CSF tests/charts have been developed and with the use of new digital screens and technologies, the new gathered data would be more precise and accurate since one would be able to reproduce accurately a certain stimulus with specific size and luminance level.

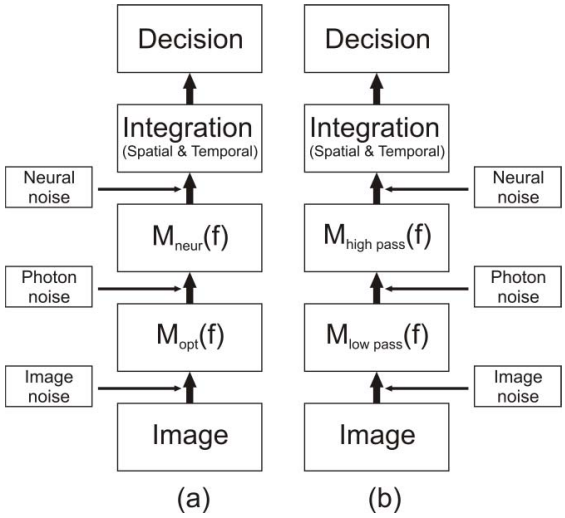

Figure 1.6: *Block diagrams of human contrast sensitivity modelling. (a) represents the usual approach with the Neural and Optical division such as the one proposed in Barten (1999). (b) represents the proposed approach in Roka et al. (2009), discerning between Low pass and High pass. The figure is taken from Roka et al. (2009).*

Lastly, the properties of the human eye present a relatively large inter-variability between each subject (eye length, refractive errors, luminance levels, lens ageing, etc.), so these models are just a general approximation that try to account for the most common scenarios.

1.2.3 Optomechanical eye models

This section will review the different optomechanical eye models developed to evaluate image quality. Contrary to the theoretical eye models, which are mainly used for the understanding of eye properties and are usually only simulated with software, these optomechanical models are in vitro prototypes fabricated and used for a wide range of applications (evaluation of intra-ocular lenses, spectacle lenses, contact lenses, post and pre-surgery evaluation, new research studies, educational purposes, optical design, etc.). Note that many of these prototypes are based on such theoretical models. They try to replicate the anatomical or functional parts of the eye, ideally with a customizable setup, due to the large inter-variability of parameters between subjects Amorim et al. (2022). In order to evaluate the performance of these models, several techniques can be used depending on the targeted outcome:

- *Purkinje images.* With this technique, the model evaluation is performed

through the four different Purkinje image reflections present in the anterior and posterior surfaces of the cornea and the lens, respectively. Since this evaluation technique only takes into account the surfaces up to the lens, these eye models do not require to have vitreous humour and retina. An example of these characteristics is found in de Castro et al. (2007), where the study mainly focuses on measuring decenters and tilt produced by intraocular lens surgery procedures. An example of the different Purkinje images observed in the cornea is shown in Fig. 1.7.

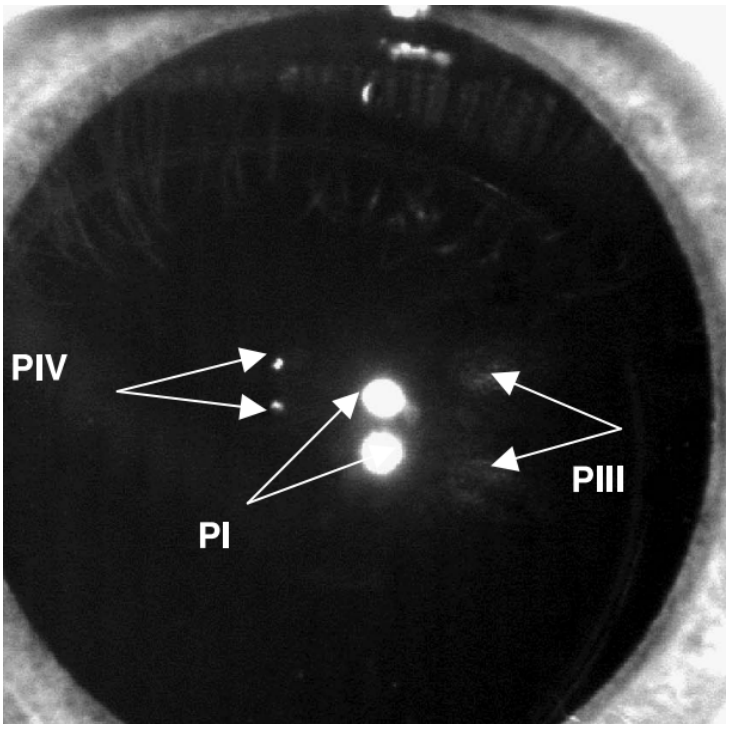

Figure 1.7: *Example of the different Purkinje images. It can be observed the reflection produced in the anterior surface of the cornea (PI), in the anterior surface of the lens (PIII) and in the posterior surface of the lens (PIV). The figure is taken from Rosales et al. (2006).*

- *Single-pass measurements.* Is the most common and widely used technique regarding these eye prototypes. The image is evaluated at the retinal surface by simply adding a sensor (charge-coupled device (CCD) or complementary metal–oxide–semiconductor (CMOS)) at the image plane. This is why it is called single-pass, since light has to go through the optical surfaces only once in order to provide an evaluation. Two main drawbacks arise with this evaluation type. The first one is the lack of realism with this image evaluation since the only real evaluation for the in-vivo eye of the retinal

image is our own visual pathway. The second one would be the linearity of the image sensors used. CCD and CMOS sensors are linear throughout the whole surface, whereas our retina photoreceptors do not provide a linear response (image quality diminishes with eccentricity). This is why is also important to implement a contrast sensitivity model while evaluating the image resolution in the retina since it will account for these non-linearities. The most common evaluation metrics for these eye prototypes would be MTF, Point Spread Function (PSF), Strehl Ratio, etc. Majority of these prototypes are developed in an optical bench. The layouts proposed in this thesis would fall under this category of eye setups in the case of possible manufacturing. Some examples using this approach would be the models proposed by Carson et al. (2014); Arianpour et al. (2013)

- *Double-pass measurements.* As its name states, these kinds of measurements have to go through the optical media twice, so the retinal image is usually evaluated by a sensor placed in front of the eye. This technique is widely used to quantify the scattering present in the prototypes since the wavefront measurements (explained below) are not able to calculate this scattering produced. A variant of this evaluation would be the *eye fundus/retinoscopy* technique since they also evaluate the light that gets reflected in the retina. It is a variant since the only useful information in this technique is the light that gets reflected from the retina.

- *Wavefront measurements.* Useful to quantify accurately the different optical aberrations of the eye model prototype. One of the most popular techniques used for wavefront evaluation is the Hartmann-Shack sensor. This device is based on small lenslets placed on a grid pattern. Each of these lenslets focuses light on a determined place in the sensor (CCD/CMOS). When focusing the light that goes through the eye prototype, there would be a certain displacement of the wavefront that is measured in order to quantify the optical aberrations caused by the system. This kind of wavefront measurement is usually performed from the cornea up to the retina with double-pass technique Prieto et al. (2000) and other prototypes measure them backwards from the retina up to the cornea. When the measurement is performed backwards it is called *second-pass measurements*, since it is evaluating the aberrations produced by the light exiting the eye while avoiding the disadvantages produced by double-pass measurements Esteve-Taboada et al. (2015). Some other prototypes, such as the one developed in Campbell (2008) permitted the possibility of single-pass measurements by replacing the retina with a transparent surface, or double-pass measurements by adding a dark diffuse surface. The setup can be observed in Fig.1.8.

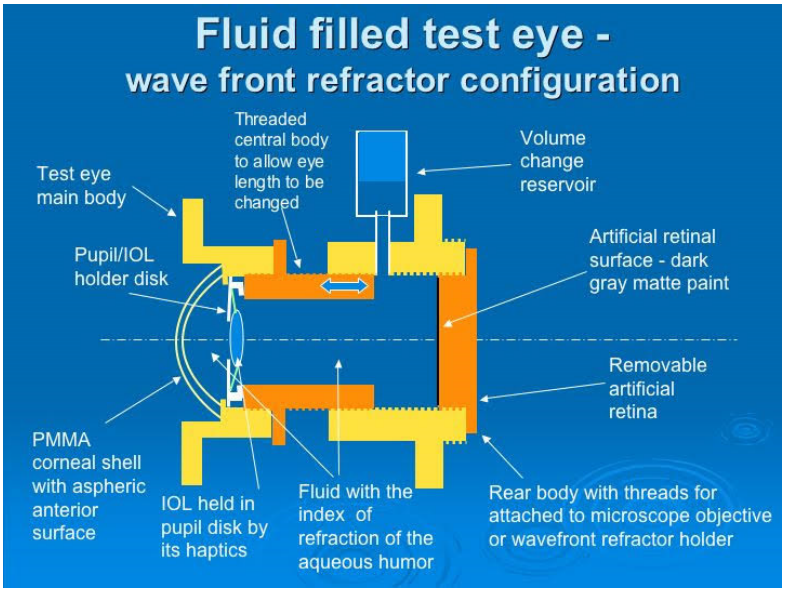

Figure 1.8: *Cross section of the eye model prototype designed by Campbell. The setup can be treated as a single-pass measurement by replacing the retina with a transparent surface, or a double-pass measurement by adding a dark diffuse surface. The figure is taken from Campbell (2008).*

The amount of developed optomechanical models found is around 80 different approaches. In this chapter will be reviewed a few of them, especially the ones that resemble the eye form factor and measure image quality through sensors (Single-pass measurements) since the approach developed in this thesis follows these characteristics. One of the first eye prototypes developed was the one by Gliddon (1929), where the main purpose of the prototype was the study of the retinal image. The device consists of a copper enclosure filled with liquid. It featured a tunable structure containing a glass replica of the retina, filled lenses with water in between to simulate the cornea and lens, and apertures to imitate the pupil. These components were able to move along the prototype, in order to produce any decenter or tilt. The image formed on the artificial retina was evaluated using an objective lens and an eyepiece. This model was considerably accurate, taking into account that it was developed in 1929 and incorporated many fundamental aspects found in future eye models.

An interesting approach was developed by Arianpour et al. (2013), where they developed a low-cost eye model in order to measure refractive errors while trying to resemble the human eye as much as possible. The model was based on Navarro's eye model parameters Escudero-Sanz and Navarro (1999) and the interesting part of this approach is that they used a curved fiber bundle to simulate the retina curvature, connected to a CMOS sensor. Since the purpose of this model is to

evaluate refractive errors in the fovea/macula, the field of view of this setup is no larger than 35 degrees, more than enough for their purpose, but not enough to imitate human wide angle field of view (FoV) (160°). This setup can be observed in Fig. 1.9.

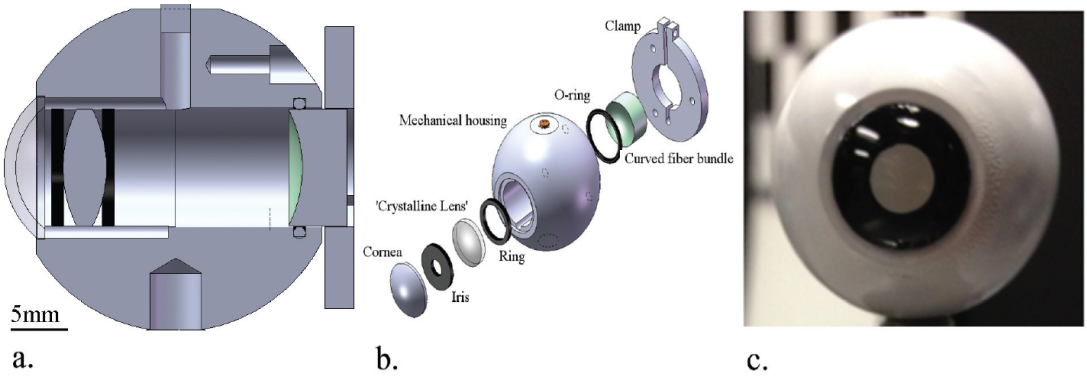

Figure 1.9: *Optomechanical eye model developed by Arianpour et al. (2013). In A, a cross section of the model is depicted. In B, all the parts compounding the setup are listed. In C, an image from the real prototype is shown. The figure is taken from Arianpour et al. (2013).*

In Liang et al. (2014), a bionic cornea and lens with a compression ring are presented, in order to vary the curvature radius of the lens. The image is collected through a CCD sensor. Spherical and axial aberrations are larger than expected in this approach. They focus the study mainly on bionic lens development. A similar approach is developed in Petsch et al. (2016), where instead of modifying the lens curvature they developed a tunable iris with soft-matter micro-optics. It ranges from 1.75 to 5.00 mm, and the MTF and depth of field (DoF) variations in this range are measured. The main drawback of this model is the narrow FoV, only 40 degrees. As observed, most of the prototypes proposed work properly for their designed function (refractive error measurement, quantify aberrations, etc.). But they neglect other eye properties when it does not compromise their aim since accounting for all of the requirements is a goal really difficult to achieve.

1.2.4 Curved sensors

One of the other challenges that arise when developing a human eye prototype is the sensor used in order to capture an image. The most common sensor types are charge-coupled devices (CCD) and complementary metal–oxide–semiconductors (CMOS), which are widely used in almost every single image-capturing device. Most eye optomechanical models reproduce retinal sensitivity responses with flat sensors,

but it would be ideal to have a curved sensor in order to reproduce the human eye's form factor as close as possible. Also, using a curved focal plane would considerably reduce the complexity of the optical setup, its optical aberrations (e.g., Petzval field curvature) and the number of optical elements needed, thus diminishing the cost and manufacturing effort Rim et al. (2008). The development of curved imaging sensors has been relatively fast in the past few years since they can lead to new innovations and improvements in the imaging industry Gao et al. (2022). Several attempts have been proposed in order to mimic a curved retina, not only in humans but also by taking anatomic ideas from aquatic animals Liu et al. (2016); Kim et al. (2020). Artificial synapse processes are also reproduced in some models, called *Neuromorphic*, since they mimic the animal neural properties Kim et al. (2022). This recent term stands for technology that encompasses the creation of computing systems and models that draw inspiration from the structure and functioning of the human brain cells and the nervous system. These systems strive to replicate as close as possible the parallel processing, energy efficiency, and adaptability found in biological neural networks. By imitating the behaviour of neurons and synapses, employing concepts like spiking neural networks, event-driven processing, and specialized hardware architectures, they aim to achieve this emulation.

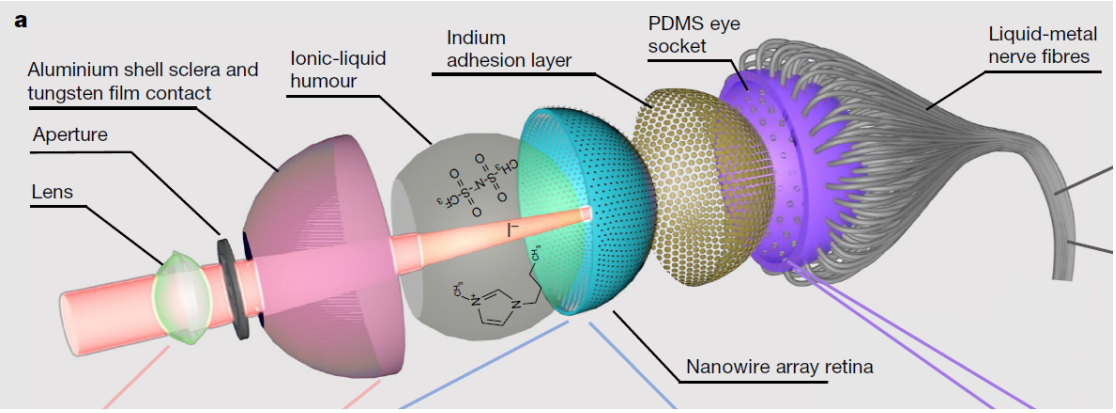

Figure 1.10: *Example of a biomimetic electrochemical eye model prototype with curved retina compounded by nanowires mimicking photoreceptors. The figure is taken from Gu et al. (2020).*

Some technological attempts to produce models of the retina have been made, such as soft optoelectronics Choi et al. (2017); Ko et al. (2008). Another interesting model is developed in Gu et al. (2020), where the anatomic similarity to the human eye is high, as well as the imaging capabilities. A biomimetic eye example of these characteristics can be seen in Fig. 1.10. The complex technology implemented in this model makes it hard to reproduce (liquid metals nerve fibres, ionic-liquid humour, etc). Simpler approaches are presented in Hugot et al. (2019); Guenter

et al. (2017), where they present the commercial and mass production possibility of curved sensors by simply applying pressures and grinding process in order to induce a certain curvature on them. These proposed sensors will be evaluated in the presented designs. In Bakaraju et al. (2010), the retina is mimicked by moving the sensor along a curve that matches the retina's radius of curvature.

1.3 Research Questions

After understanding the human eye characteristics, anatomy and imaging properties, all the required constraints for our model will be set. In this master thesis, a procedure for designing an eye model prototype will be followed in order to answer the following research questions:

1. In an artificial eye model, how can human vision be reproduced as simply as possible, while respecting the eye's form factor and achieving good imaging resolution?

2. Is there a significant difference in the implementation of a flat sensor vs. a curved sensor in order to simulate the retina?

3. Which are the main problematic optical aberrations for the designs under study?

2 Materials and Methods

2.1 Eye constraints

As observed in Chapter 1, designing and optimizing a human eye prototype can be a challenging task. Let's identify the main surface challenges in summary:

- Cornea: It is crucial to have a good model for the shape of the first surface of the eye since it is the one where there is a strong refractive index change and spherical aberrations may be induced. The cornea is an aspherical surface with an average radius of curvature of 7.7 mm and an aspheric factor of -0.26 in the anterior surface and 6.8 mm radius of curvature and -0.31 aspheric factor on the posterior surface. This aspheric/conic factor (K/Q) is later explained in surface types section. The cornea's central thickness is around 0.55 mm. These parameters can be observed in Fig. 2.1. Previous models have reported to use polymethylmethacrylate (PMMA) material to replicate the cornea. The model in Bakaraju et al. (2010) reported to use a material with exactly the same refractive index as the cornea in the theoretical Gullstrand eye model (1.376 for a central wavelength of 587 nm). When mimicking this surface with glass, the typical material used is BK7, with a refractive index of 1.516, a bit higher than the cornea. The main drawback of using this surface will be the spherical aberration since it is assumed a spherical surface, and the refractive index is higher than with PMMA or other materials. Some other models also reported using different materials such as silicones, or filled liquid lenses. Regarding the posterior surface of the cornea, the constraints can be more relaxed, since the contribution to the eye performance is quite small. This is due to the small fluctuation of refractive index between this surface and the aqueous humour. An accurate cornea model will be required in order to achieve an accurate entrance pupil size to follow the human vision behaviour.

- Pupil: This element is mainly responsible for the amount of light entering through the system. It is also responsible for the diffraction increase for low

pupil sizes and optical aberrations for high pupil sizes. This surface is usually represented in the models as a circular iris with a certain diameter. Some prototypes are able to modify this diameter Petsch et al. (2016), in order to measure the aberrations present at different sizes, and also to reproduce photopic, mesopic and scotopic conditions. This variability of diameters usually ends up in a more complex setup. For simplicity, in the developed model eye models in this thesis, an average entrance pupil size of 3.5 - 4 mm is established, trying to establish an average pupil size for photopic-mesopic light conditions.

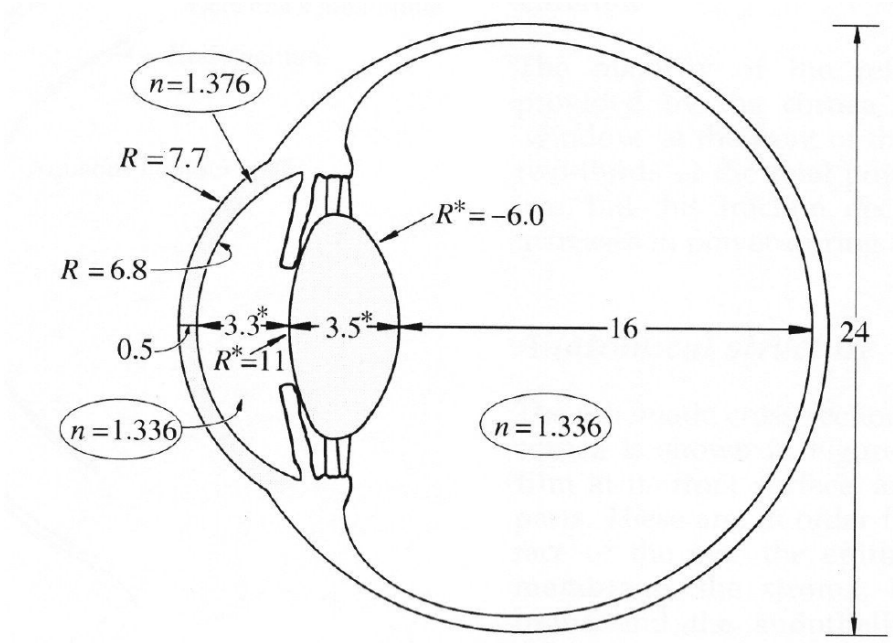

Figure 2.1: *Representation of the human eye with the corresponding refractive indices, average radius of curvature for each surface and average length in millimetres. This represents the eye in relaxed accommodative parameters. The values marked with an * are prone to change when accommodated. The figure is taken from Atchison (2023).*

- Retina: Since the model will be focused on the imaging capabilities of the eye, several focal plane arrays will be tested for the model. Curved and flat ones. The image size will be extended up to a diagonal of 28 mm approximately (22.58 x 16.89 mm) according to sensors available in the market (CMV12000 CMOS sensor) that are able to reproduce determined curvatures and image sizes. Ideally, this image sensor size shall be minimized. The aim is to have a simple and reliable model capable to achieve the same or better resolution

than the human eye, also keeping in mind that the neural noise will be induced to the achieved quality in the model.

- Others: For the rest of the eye components (lens, anterior and posterior chamber) the scope of the prototype does not focus on replicating exactly each surface of the eye, but to acquire a similar image quality. Several surfaces and glasses will be tested in order to achieve this objective. Since the focus is aimed at the imaging capabilities of the system, while trying to respect its appearance, one of the main constraints on this eye prototype will be to respect the overall length (OAL). According to several studies Bhardwaj and Rajeshbhai (2013); Roy et al. (2015); Hitzenberger (1991), the axial length of the eye is defined as the distance that goes from the outer layer of the cornea (epithelium) up to the outer layer of the retina (Bruch's membrane). This length is usually measured by interferometry methods or retinoscopy techniques. The average axial length of the human eye is approximately 24-25 mm, and in some cases goes up to 28-29 mm for myopic eyes and around 22 mm for hyperopic eyes. According to these values, the range to work in the design will be from 22 mm up to 29-30 mm. For the consistency of the eye model prototype, the diameter of the lenses used cannot either surpass this axial length(28-30 mm), otherwise, the prototype will not resemble the human eye design. In Fig. 2.1 are depicted all the main anatomical eye parameters.

2.2 CODE V

The implementation of all these constraints and the design of the eye model prototype will be carried out in CODE V optical simulation software, developed by Synopsys Synopsys, Inc. (2023). CODE V is a software mainly used for the design, analysis, visualization and optimization of optical systems, photonic or telecommunication systems and illumination systems. It offers a wide range of tools. Here will be explained only the ones used for the eye prototyping, since the range of applications of this software is quite wide.

2.2.1 Environment

The environment of the program is depicted as follows. On the left side of the screen, it is found the navigation window which provides access easily to all the windows running while using the program (see Fig. 2.2). In the upper part, fast access to the different tools is provided, to save the model, export an existing design, visualize the design, etc. There are three windows that are already opened

when running the software. The command window, where you can write all the desired commands. It is basically the workspace. Next, is placed the error log window, where any error happening while using the software will appear here to warn the user.

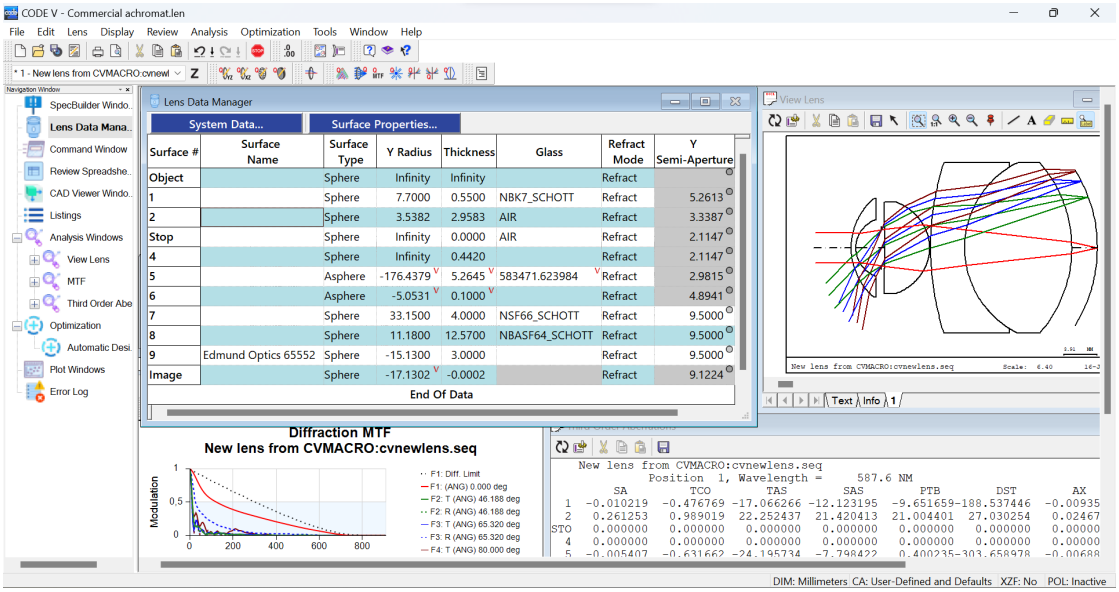

Figure 2.2: *Screenshot from the CODE V optical simulation software. The figure is taken from Synopsys, Inc. (2023).*

The third window opened is the Lens Data Manager. All the different surfaces present in the design will be settled in this space. The first column in this window (Surface #) describes the surface number. it simply indicates the number corresponding to each surface, the object, the aperture stop and the image. In surface name, it can be established a determined caption for a surface or a group of surfaces. It is used when a catalogue lens is imported from a fabrication manufacturer (ThorLabs, Edmund Optics, etc). The third column corresponds to the surface type. Here the user can select over a large number of surface types. This eye model design presented will be restricted to the use of either spheric, conic or aspheric surfaces:

- Spheric. This kind of surface accounts for a curvature that has the surface shape of a sphere. Is the most common type of lens and is widely used for lenses and mirror design. The main parameter here to modify is the desired radius of curvature (R). The smaller the radius of curvature is, the more curved surfaces are achieved and the larger the radius the more flat surface is obtained (keeping in mind that a flat surface is a spherical surface with an infinite radius of curvature).

- Conic. This surface type is developed by rotating a conic section around its axis. A new parameter is presented, the Conic/Aspheric constant (K). Depending on this value there will be three different types of surfaces:

  - Ellipsoid. With a positive K value (K>0), and values up to -1 (-1 < K < 0). The human eye cornea would fall under this category, since it has an anterior and posterior conic value of -0.26 and -0.31, respectively.
  - Paraboloid. A value of K=-1 specifies them.
  - Hyperboloid. Values ranging from K < -1 account for hyperboloid.

  A spherical surface would also be a specific case of conic, with a K value of 0. For a better understanding, a schematic view of the different conic shapes is represented in Fig. 2.3.

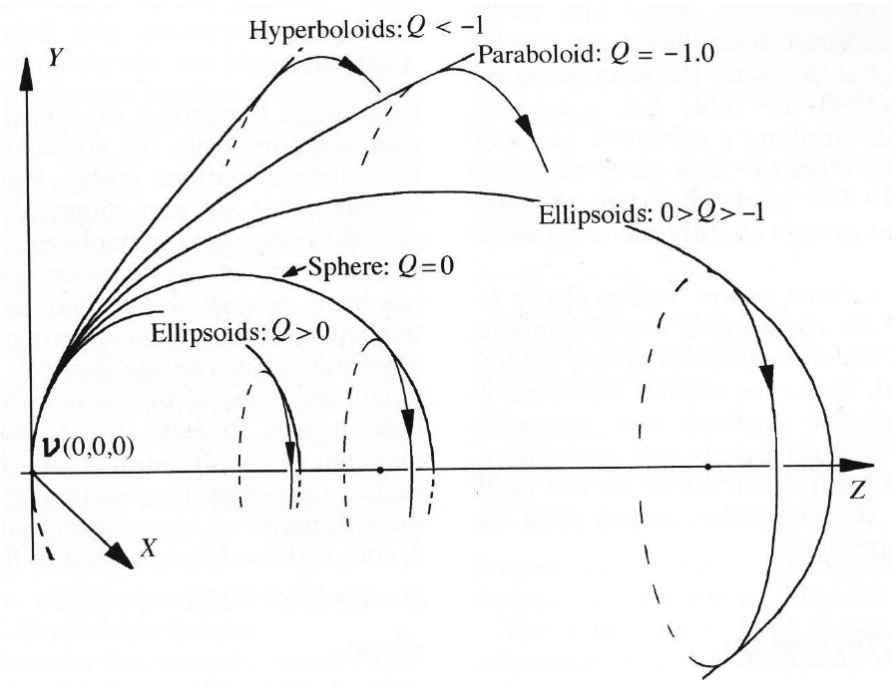

Figure 2.3: *Conic shapes depending on the conic factor (K). The figure is taken from Atchison (2023).*

- Aspheric: This kind of surface is a bit more complex than conic or spheres. They have a changing curvature profile along their surface. High-order coefficient parameters are introduced, up to 20. Aspheric surfaces are mainly devoted to reduce optical aberrations, thus improving the performance of

the optical system. An aspherical surface is depicted through the following formula:

$$z(r) = \frac{cr^2}{1 + \sqrt{1 - (1 + K)\, c^2 r^2}} + \sum_{i=2}^{n} A_i r^{2i} \tag{2.1}$$

where:

z is the sag of the surface at a radial position r,
c is the curvature of the surface (primary coefficient),
K is the conic constant,
r is the radial distance,
A_i are the higher-order coefficients,
n is the highest order considered.

Almost another 30 different surface types are available on the software, but as specified before, only sphere, conic and asphere will be explored for the prototypes. Ideally, only spherical surfaces are used to maintain the design simple, but aspherical and conic surfaces will be introduced to reduce aberrations and increase performance.

The fourth column in Fig. 2.2, references the radius of curvature of the different surfaces. The fifth column 'Thickness' references the lens size and the distance between elements. The sixth column references the glass used in the lens. Depending on the Abbe number and the desired refractive index, it will be introduced a different material. Air can also be used as a material, or leaving a blank space will be also considered as air. The material used can be real (directly from the catalogue) or fictitious (customized refractive number and Abbe number). If the material is fictitious, then will be approximated with the glass fitting settings of the software. Note that the values are provided in XXXX.YYYY format. The X parameters refer to the refractive index (1.XXX) and the Y values to the Abbe number (YY.YY). The Abbe number makes reference to the wavelength dispersion through the material. A low Abbe number will indicate a high dispersion and vice-versa. Usually, these Abbe values and refractive index values are indicated for the Fraunhofer lines 486.1 nm, 589.3 nm and 656.3 nm. Since these parameters are wavelength dependent. The seventh column in Fig. 2.2 indicates whether there is a refractive or reflective surface. Since eye properties are being mimicked, only refractive surfaces are considered. In this column will appear a small icon in the upper right of each box when diffractive properties are used. The last column indicates the semi-aperture of the surface, in other words, the lens size.

2.2.2 Optical design workflow

Once explained the basic setup of the software, an explanation concerning the procedure for the optical design of a human eye inspired lens is given in this section. An overview of the workflow is shown in Fig. 2.4.

2.2.2.1 Set different parameters

Before starting the lens implementation, the user also has to set different parameters in CODE V's 'Lens Data Manager ->System Data' section:

- Entrance pupil. It is established in the pupil section. In this case, it will be established around 3.5 - 4 mm average values for not obtaining too much diffraction, nor optical aberrations.

- Wavelenghts. It is also needed to establish at which wavelength range the system will operate. In the beginning of the prototype modelling, for simplicity, a monochromatic system was developed, with a wavelength of around 555 nm since it is the value at which the human visual system is the most sensitive. Once a relatively good accuracy was achieved, it was modified to a trichromatic range, in order to resemble as close as possible to the human eye. These wavelengths were also established according to the Fraunhofer lines (656 nm, 589nm and 486 nm, respectively). The weight provided to the central wavelength was superior to the other ones since the eye is more sensitive at central wavelengths ($\approx$ 555nm).

- Fields/Vignetting. Several fields are represented in the design to mimic the human eye's field of view (FoV), up to 80 degrees (80x2=160°). Visual acuity is also considered here to mimic human eye resolution. The weight given to the central field (0°) is higher than the periphery fields (6-5 to the central field and 0.1 or less for fields larger than 20° eccentricity).

- Others. The main constraints to start the design are settled. Some other parameters are established in system settings, such as the temperature (22°C), the pressure (760 mmHg) and the units of the design (mm).

Another useful software tool for the prototype is the SpecBuilder, where a table can be set to visualize the different constraints for the design altogether. Is a fast way to check that the right way is being followed. After all the mentioned steps, the desired eye model can be started, testing different surfaces, thicknesses, materials, curvatures etc.

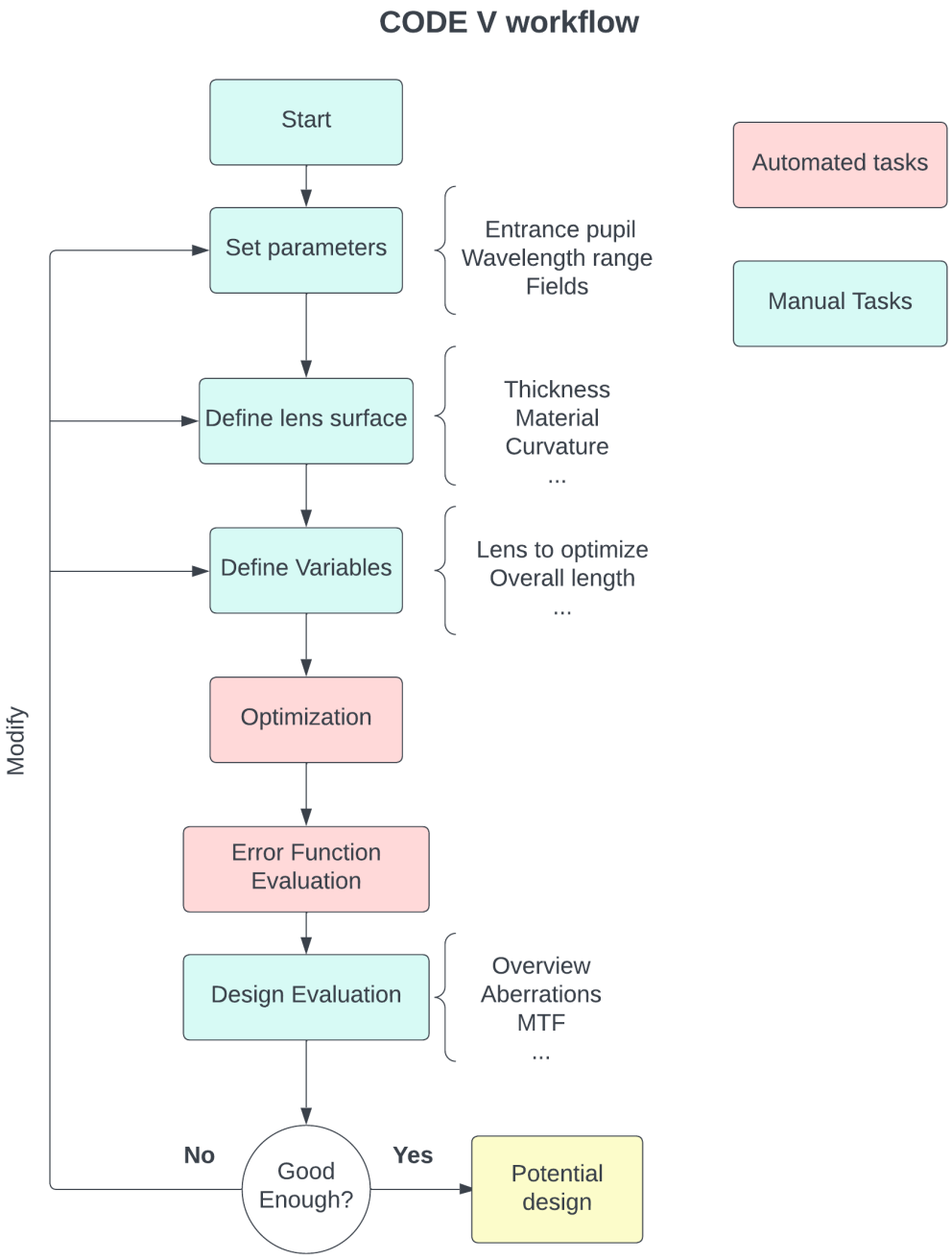

Figure 2.4: *Workflow followed in CODE V software*

2.2.2.2 Lens setup

The first element established in the design will be the cornea. The parameters established by Allain and Thibault (2022) will be adopted in order to match the Chromatic Aspherical Gullstrand Exact (CAGE) model, since it is of crucial importance for an accurate entrance pupil's appearance. It is known that the pupil entrance adopts an ellipsoidal shape (see Fig. 2.5) when viewed off-axis and some other distortions and tilt appear when viewed from far off-axis Fedtke et al. (2010); Aguirre (2019). After this, a wide range of surfaces after the entrance pupil will be tested, including thicknesses, materials, curvatures etc. The different experiments and lens setups achieved will be described in Chapter 3.

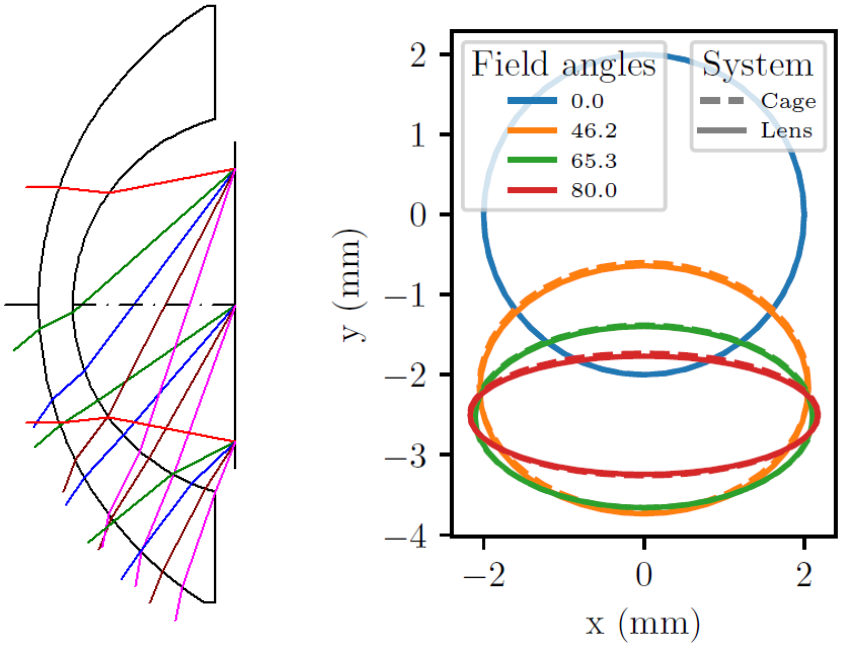

Figure 2.5: *Cornea lens surface designed in the left. Each color accounts for a fan of rays entering the system with a determined angle. Entrance Pupil projection for each field (indicated with different colors) compared with the CAGE model in the right. The images are obtained from the design procedure developed by Allain and Thibault (2022)*

2.2.2.3 Optimization

Once there is a potential design that could be improved, the optimization part plays an important role in the design of the model. This process is ruled by a merit or error function where the objective is to have it minimized. The smaller

this value, the closer the design is to the desired image quality requirements with determined constraints. The aim of this optimization process is to achieve an optimal design within a determined range of constraints. In CODE V this option is called Automatic Design. It works by using a damped least square algorithm and Lagrangian multipliers (adding constraints when needed) in order to improve the system. This optimization is performed to the desired parameters able to change (curvature, thickness and material) by simply adding the option 'vary' to the element. It will appear with a red 'V' in the upper right corner of the parameter, indicating that this parameter is prone to be modified (see Fig 2.2).

There are four different predefined types of error functions: Transverse ray aberration, MTF, wavefront error variance and Fiber coupling. The main one used is Transverse ray aberration, which basically provides the Root Mean Square (RMS) minimum spot size of the image. In other words, the deviation of light rays from the ideal path. CODE V also allows the implementation of custom merit functions and seeing the optimization process in each cycle performed with the corresponding Error function variance. Another optimization mode can be used, called Global Synthesis. It may expand the number of possible solutions provided by the usual optimization process. Several constraints are also added while performing the optimization process:

- In the general constraint section, it will be established a minimum element center thickness of at least 1 mm, a minimum air center thickness of, at least, 0.1mm (separation between lenses in the central axis) and a minimum edge thickness of 0.02 mm. This is settled in order to keep a realistic design for its later possible manufacturing. Sometimes in this optimization process, quite unrealistic layouts are proposed. Optical elements too thin or with impossible shapes have to be penalized during optimization.

  The glass map boundary used will be the default one established by the software, a four-sided glass map boundary, (NFK5 NSK16 NLAF2 SF4). It can contain up to 5 glass types. In this map, the 4/5 different glasses form a polygon. The glasses falling inside this polygon will be the ones tested in the optimization process. The whole map of the different types of glass can be observed in Fig. 2.6.

- In the specific constraint section, a wide range of different constraints could be included. The main one included here will be the Overall length (OAL) not surpassing 30 mm. It may also be included an effective focal length (EFL) of 17 mm (similar to the human eye) in order to have a resolvable center resolution, and different diminution of Third order aberrations (Spherical, Coma, Astigmatism, Distortion or Petzval curvature).

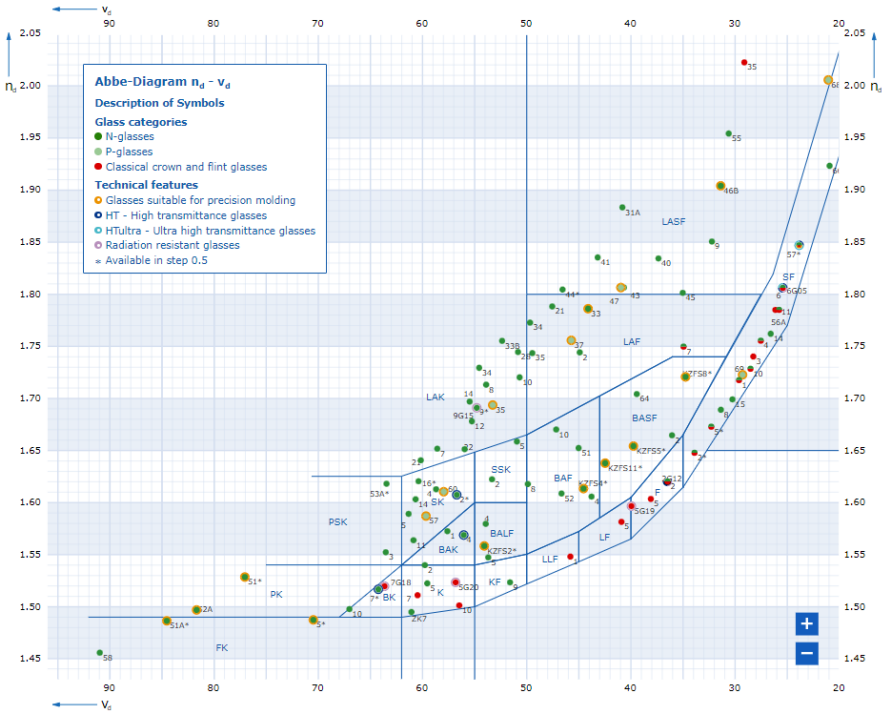

Figure 2.6: *Abbe diagram of the different Schott glass types. The Abbe number is plotted vs the refractive index. Each dot in the plot represents a specific glass type. The image is retrieved from Schott (2023)*

2.2.2.4 Evaluation

After performing the optimization process, an evaluation of the design is done. This evaluation will be performed by looking at several parameters:

1. Overview. Firstly, a general look checking that the overall length is acceptable and does not overpass 30 mm, the quick lens view and ray tracing seem realistic, the curvature, thickness and diameter of each lens are fine and the image size is not too wide for the later sensor implementation.

2. Aberrations. There is no perfect optical lens setup. Aberrations always arise to a greater or lesser extent. An aberration analysis is carried out in CODE V by evaluating the third order aberration values. The third order aberrations evaluated are mainly:

    - Spherical aberrations (SA). Rays going through a lens ideally merging in a point, converge in a determined area.
    - Tangential Coma (TCO). Usually due to marginal rays in the system, focusing on a different off-axis point than expected.

- Tangential and sagittal astigmatism (TAS/SAS). Astigmatism occurs when the tangential and sagittal focus do not coincide in the same focal plane.
- Distortion (DST). The image of an off-axis point is focused closer or further to the axial focal point. There are two types: Barrel (-) and Pincushion (+). Due to the curvature and the wide FoV, distortion negative (barrel) values will be always high in all the proposed designs, but this is expected since it is also present in the Human visual system.
- Axial color (AX). Also called axial chromatic aberration (transverse and longitudinal), is basically the difference of focus depending on the wavelength.
- Lateral color (LAT). This is referred to the image height focus depending on the wavelength. It is also called *chromatic difference of magnification* Smith (2008).
- Petzval curvature (PTZ). Also called field curvature, causes the image field plane to be curved. This is one of the main aberrations that can be easily corrected with a curved sensor.
- Petzval blur (PTB). It quantifies the blur or defocus caused by the field curvature.

  Note that all these aberration values will be provided in millimetres (mm) when discussing the results obtained in Chapter 3.

3. Modulation transfer function (MTF). The main graph to look at while optimizing will be the MTF. It gives a fast overview of the image quality and will provide a hint that the desired way is being followed. It is also useful to see the performance achieved in every field (see Fig. 3.1c as an example). It is provided in cycles/mm or cycles/deg. Note that CODE V provides two types of MTF evaluation: Geometrical MTF and Diffraction MTF. Geometrical MTF is limited to evaluate the effects caused by geometric optics (optical aberrations). In diffractive MTF the evaluation is performed taking into account the previous parameters and the effects caused by diffraction in the system, thus providing a more complete examination of the system. Diffraction MTF is one used in the performance analysis of the different setups.

4. Customized Contrast threshold (C_{thresh}). Measured in cycles per degree and compared with the human eye CSF cutoff frequency (60 cycles per degree) developed in Allain and Thibault (2022) will be also used to evaluate the design (see Fig. 3.1b as an example). The threshold frequency (C_{thresh}) is

defined as a contrast sensitivity (CS) of 1 and means that a modulation of 100% is needed to detect the modulation Allain and Thibault (2022). The aim is to be similar to the HVS requirements or over it (at least 10-25% for the center MTF in 60 cycles/degree), since here the induced neural noise explained in Chapter 1 is taken into account (green curve in 3.1b, is an example showing this MTF limit). This graph follows the CSF developed by Barten model Barten (1999), whereas the previous MTF plot only provides an overview of the image quality obtained through the visual path (different lens setup).

5. Others. Some other graphs provided by CODE V may be used. The Spot size diagram tells how distorted the image gets at each field and for each wavelength. The relative illumination entering the system is useful when modifying the vignetting, in order to make sure that it is not provided less illumination for any field if compared with the human eye. This extra information regarding the proposed eye model designs can be found in Appendix A (Figs. A.8 and A.9, respectively). Lastly, a fast 2D image simulation with real images to see how the vision will look like through the optimized optical system.

Table 2.1: *Summary of the different constraints required for our proposed designs.*

List of constraints	
Overall length (OAL)	Between 22 and 30 mm
Effective focal length (EFL)	Between 17 and 20 mm
Field of view (FoV)	160 degrees
Entrance pupil diameter	3.5 - 4 mm
Entrance pupil shape 80 degree field	Shall follow CAGE model
Center MTF frequency	60 cycles/degree
Center MTF	10 to 25% contrast @ 60 cycles/degrees
Sensor size	No larger than 28 mm
Sensor curvature	Radius 3 times larger than sensor size
Aberrations and surface number	Minimized

Once performed all this workflow, it is considered if the system is good enough or if, on the contrary, it does not fulfil the desired requirements. If not, this workflow shall be repeated as many times as needed. If yes, a potential design has been developed. In table 2.1 are summarized all the requirements and constraints previously discussed in this section, that are required for a good eye model. The software tools and procedures explained here are the ones used for this specific

optical design. The tools and capabilities of CODE V are wide and can be used to any other extent, but here the explanation is limited to concepts regarding the restricted eye model proposed.

3 Experiments, Results and Discussion

After getting familiar with CODE V, learning and understanding all the necessary techniques for optical modelling in it, the next step will be to start modelling designs having in mind the constraints and requirements previously presented in Table 2.1. This chapter will show the design trials performed, and the procedure followed until potential results are achieved. The full list of parameters for the replication of each proposed design under evaluation can be found attached in Appendix A (Figs A.1 - A.7). The rest of the designs included in this results section (Designs 2, 3, 4-7, 9-12, 16-19, 21 and 22) provide a general idea of how the design process was carried out but are not fully evaluated since the parameters from the already discussed designs are only slightly different.

3.1 Starting point

The starting point will be the design presented in Allain and Thibault (2022), in order to have a first overview of the model, see the different constraints compounding it and see how it can be improved. The provided setup is presented in Fig. 3.1. As observed in Fig. 3.1a, the setup consists in six spherical lenses, where two of them are doublets. The sensor is flat with a size of 12.6 mm, an entrance pupil size of 3.5 mm and an axial length of 26.57 mm. Note also that this setup presented was monochromatic, taking only into account a central wavelength of 585nm. In Fig. 3.1b is represented the Human Visual System (HVS) contrast sensitivity function in comparison with the CSF of the setup. It is provided in cycles/degree according to the cutoff frequency of the HVS (60 cycles/degree) in the central (0°) field. As can be observed, the performance achieved by the design is higher than the human sensitivity threshold. In Fig. 3.1c, is provided the Optical MTF achieved by the system for every field in cycles/degree. It can be observed that the system resolution decays drastically for the periphery, but the requirements are still met, in accordance with the HVS, since the visual acuity in the periphery is also reduced.

The aim now will be to achieve a more relaxed system by removing some surfaces while still obtaining HVS requirements.

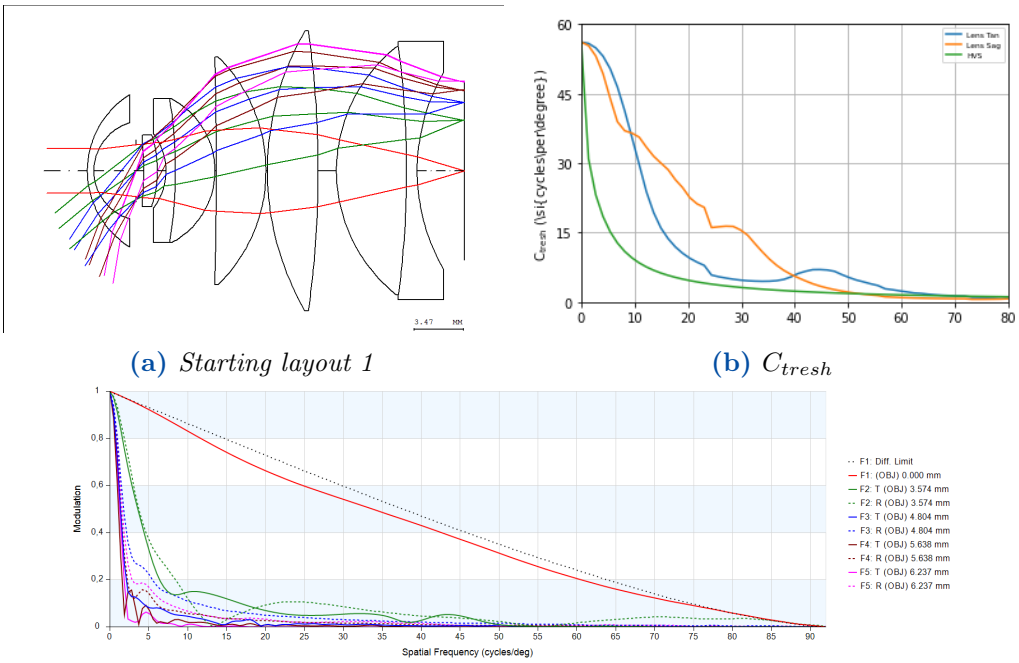

(a) *Starting layout 1* **(b)** C_{tresh}

(c) *Optical MTF*

Figure 3.1: *Initial setup developed by Allain and Thibault (2022). In (a), light propagates from left (cornea) to right (retina). In (b), C_{tresh} cycles vs degree is presented, with HVS (green line) vs Design (blue/orange line) performance. In (c) is plotted the diffractive MTF of the system (diffraction limits the best performance that can be achieved).*

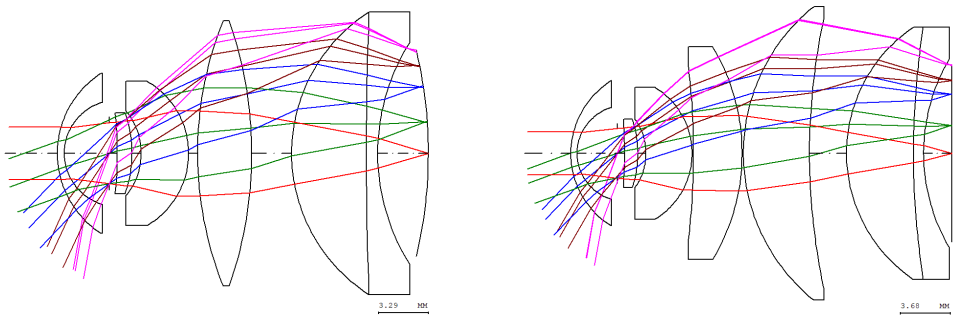

(a) *Lens layout 2* **(b)** *Lens layout 3*

Figure 3.2: *Improved designs. Light propagates from left (cornea) to right (retina).*

After several trials and errors trying to simplify the setup while still obtaining good resolution, some potential designs were constructed, represented in Fig. 3.2. In the first trial (see Fig.3.2a), a curved focal plane array (FPA) is tested, the fifth lens of the starting setup has been removed, along with the doublet setup of the third lens. Axial length has been reduced up to 24.5 mm. The aberrations were a bit increased, as observed in Table. 3.1, and the imaging capabilities were decreased. In order to minimize the aberrations and to meet totally the requirements, the fifth lens was added back to the design, whereas the doublet setup was also removed (See Fig. 3.2b). A flat sensor of 13.02mm is placed back. Requirements now are met again and aberrations are considerably reduced. With this lens removal procedure, it has been proved that is possible to still achieve a potential design with less number of surfaces, thus way more simple.

Table 3.1: *Third order aberrations obtained for potential monochromatic setups 1, 2, 3, 7 and 8. The aberrations obtained for the rest of the designs can be found in Table 3.2. The best values achieved (i.e., values closest to zero) for each aberration have been marked in red.*

Third order aberrations							
Design	SA	TCO	TAS	SAS	PTB	DST	PTZ
1	-0.017	0.168	-0.562	-1.558	-2.056	-458.9	-0.013
2	-0.006	0.08	-11.37	-6.255	-3.694	-559.3	-0.021
3	-0.005	-0.038	-3.062	-1.982	-1.442	-546.3	-0.008
7	-0.009	-0.395	0	0	0	-546.0	0
8	0.004	-0.017	-1.544	-3.172	-3.986	-470.3	-0.019

3.2 Monochromatic design from scratch

The aim now is to achieve a simpler and more relaxed design able to meet the imaging requirements for the HVS, that is why a new design from scratch is proposed. Lenses will be added gradually, considering the parameters to fix and solve step by step. The same constraints are established for the design, as well as the first surface parameters. For initial simplicity, these first trials are also developed monochromatic (central wavelength 555nm). The starting design consists only of two spherical lenses with a curved FPA and high resemblance to the anatomic human eye, as depicted in Fig. 3.3a. The image performance achieved is very low (MTF, C_{thresh}), as well as the aberrations (see Table A.1) and the curvature of the sensor in the design cannot be reproduced by commercial sensors.

New designs are presented in Figs.3.3b, c and d. An aspherical lens was tested in order to decrease aberrations and increase imaging performance. The aspherical

parameters optimized are the conic constant and the first high-order coefficient (A). Another spherical lens was also added in 3.3c, d and e in order to reduce the OAL and the sensor size. Relatively good results regarding aberrations were obtained for layout 7 (See Table 3.1), where almost null aberrations are achieved apart from a slight TCO and SA, but the OAL achieved is larger than the 30mm constraint.

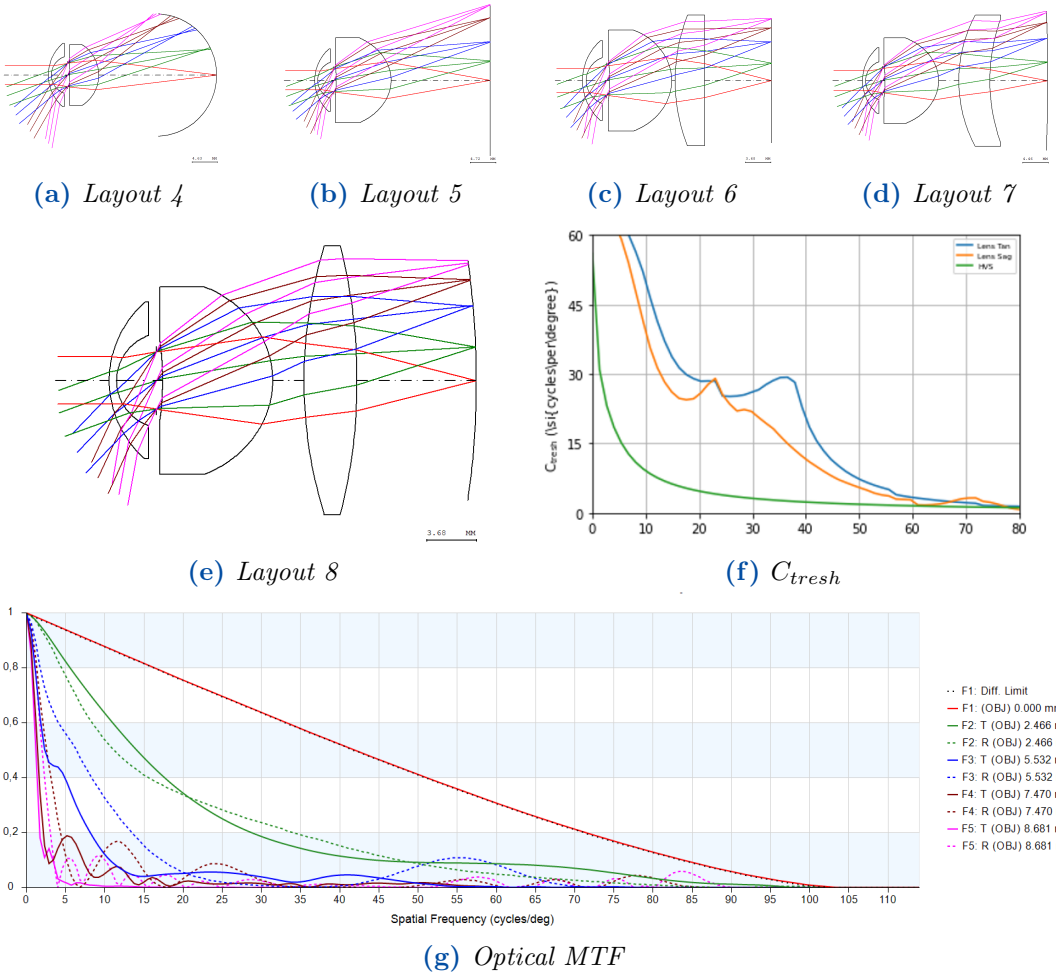

(a) *Layout 4* **(b)** *Layout 5* **(c)** *Layout 6* **(d)** *Layout 7*

(e) *Layout 8* **(f)** C_{tresh}

(g) *Optical MTF*

Figure 3.3: *Monochromatic designs. In (a)-(e), light propagates from left (cornea) to right (retina). In (f), C_{tresh} cycles vs degree is presented, with HVS (green line) vs Design (blue/orange line) performance. In (g) is plotted the diffractive MTF of the system (diffraction limits the best performance that can be achieved).*

The final monochromatic setup is presented in Fig. 3.3e. The image focal plane has been also optimized, achieving a curvature radius of -61.36 mm for a sensor size

of 17.7 mm and a OAL of 27.17mm. Layout 8 has a possibility to be manufactured. The Contrast HVS threshold criteria is fulfilled with large advantage (See Fig. 3.3f.) Regarding the aberrations (see Table 3.1), low values are achieved. The largest ones are SAS of -3.1 and a PTB of -3.98 (see table 3.1).

This monochromatic setup has proved to have promising results and performance and would be a potential design to be implemented since it meets all the required constraints imposed. It is true that the use of an aspheric lens is proposed, moving from an all-spherical setup to an aspheric one, but it may also be considered the potential diminution of lenses. Only three singlet lenses have been required, compared to the four singlets and two doublets proposed in Fig. 3.1a.

3.3 Conversion to polychromatic

To have a realistic model that follows the HVS characteristics, at least a trichromatic design is required, covering the visible wavelength range that the eye is capable to distinguish. Having as a starting point the final monochromatic design proposed in Fig. 3.3e, a polychromatic environment is proposed, trying to fulfill again all the requirements while also not trying to make it too complex or requiring too many aspheric surfaces. The wavelengths were established according to the Fraunhofer lines (656 nm, 589nm and 486 nm, respectively) as explained in section 2.2.2.1. The first polychromatic setups were designed following the previous accurate monochromatic setup architecture.

As observed in Fig. 3.4a-d, several setups following the monochromatic architecture were tested, but none of them achieved good performance to be evaluated. The starting point was three lenses, where the posterior surface of the second lens is conic. The rest of the surfaces were spherical. An aspherical setup was obtained in layout 12, but the performance was not improved enough to maintain this aspheric design. The best performance model is shown in Fig. 3.4e, with a conic lens (2nd one), but if the contrast threshold is observed (see Fig. 3.4f), it does not meet the HVS criteria for any of the angles, nor the optical MTF performance. Overall length (OAL) values and sensor sizes were all inside the allowed range, and the aberrations values achieved were not too high, mostly the astigmatism obtained were the highest aberration values, peaking with a Tangential astigmatism (TAS) of -7.798 (See Table. 3.2).

More designs were also developed trying to reach the effective focal length (EFL) of the HVS (17 mm), but the sensor sizes and diameter of the lenses achieved for this EFL value were too large (diameters of around 40 mm). Some other designs and ideas are presented in the following chapter since the polychromatic performance achieved is still low by far. Following the same architecture layout as the monochromatic setup does not seem to work for these constraints, so it may be

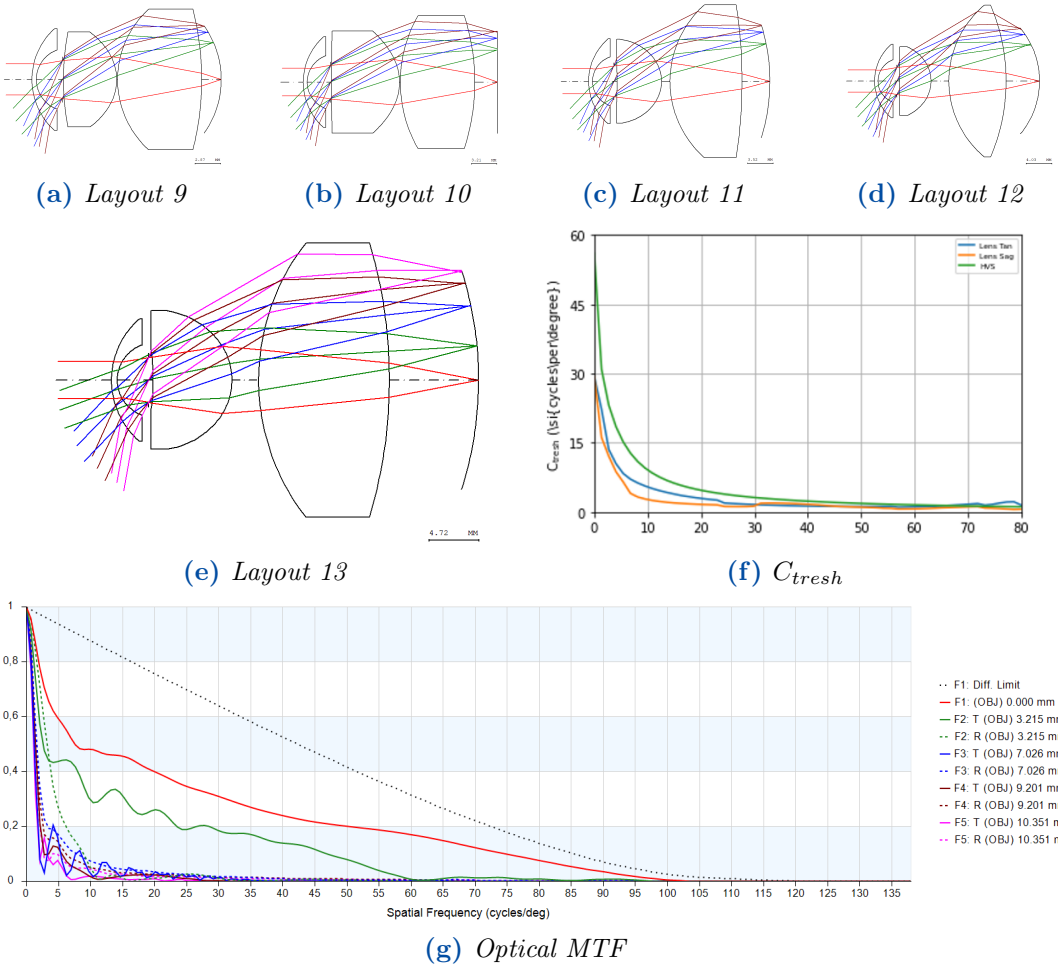

(a) *Layout 9* **(b)** *Layout 10* **(c)** *Layout 11* **(d)** *Layout 12*

(e) *Layout 13* **(f)** C_{tresh}

(g) *Optical MTF*

Figure 3.4: *Polychromatic designs. In (a)-(e) light propagates from left (cornea) to right (retina). In (f), C_{tresh} cycles vs degree is presented, with HVS (green line) vs Design (blue/orange line) performance. In (g) is plotted the diffractive MTF of the system (diffraction limits the best performance that can be achieved).*

also considered another layout.

3.4 Achromat implementation

Since the main problem with polychromatic designs is the wavelength dispersion in the image plane, causing larger aberrations and less image quality, some achromat lenses will be tested in order to see if the performance acquired is higher than the one achieved in section 3.3.

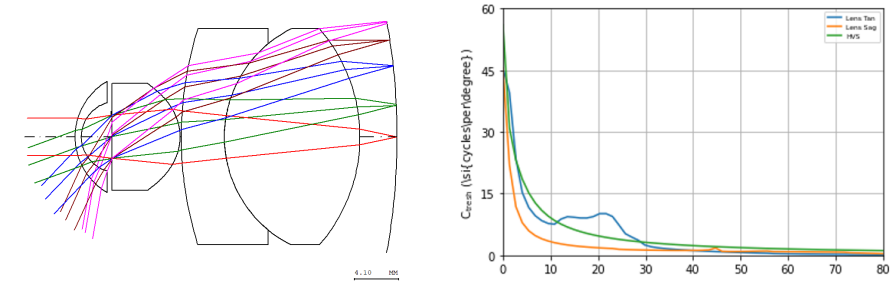

(a) *Lens layout 14*

(b) C_{tresh}

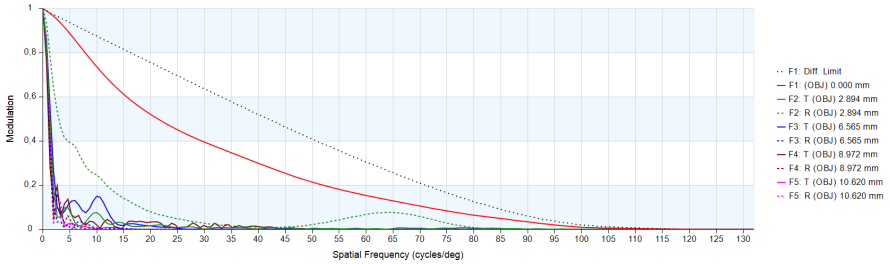

(c) *Optical MTF*

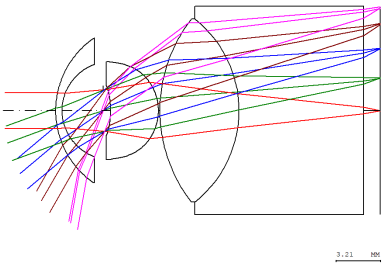

(d) *Lens layout 15*

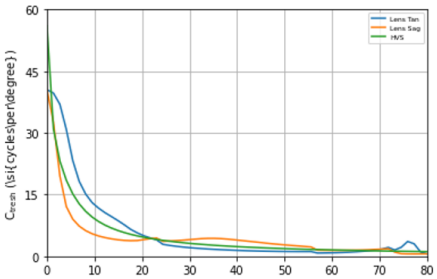

(e) C_{tresh}

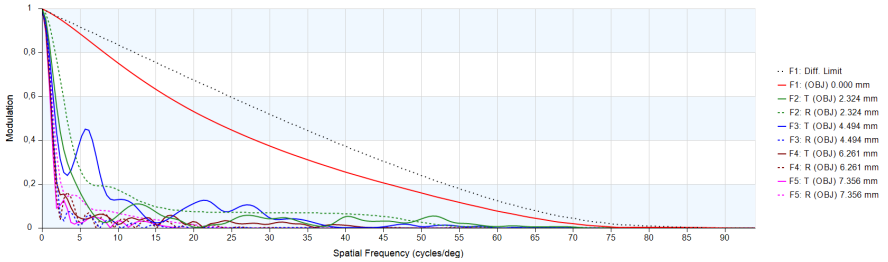

(f) *Optical MTF*

Figure 3.5: *Achromatic doublet designs. In (a), (d), light propagates from left (cornea) to right (retina). In (b) and (e), C_{tresh} cycles vs degree is presented, with HVS (green line) vs Design (blue/orange line) performance. In (c) and (f) is plotted the diffractive MTF of the system (diffraction limits the best performance that can be achieved).*

Table 3.2: *Third order aberrations obtained for the polychromatic discussed designs 13, 14, 15, 20 and 23 respectively. The aberrations obtained for the rest of the designs can be found in Table 3.2. The best values (i.e., values closest to zero) for each aberration have been marked in red.*

Third order aberrations									
Design	SA	TCO	TAS	SAS	PTB	DST	AX	LAT	PTZ
13	-0.032	-0.277	-7.798	-5.378	-4.168	-683.3	-0.049	-0.942	-0.015
14	-0.166	-0.796	0	-10.58	-15.87	-526.8	-0.003	-0.627	-0.059
15	-0.008	1.409	0	-5.222	-7.834	-511.7	-0.005	-0.429	-0.036
20	-0.008	-0.253	-15.54	-13.38	-12.30	-763.5	0	-0.551	-0.040
23	-0.007	0.755	0	-5.301	-7.952	-504.6	-0.041	-0.915	-0.038

The first potential design proposed is depicted in Fig. 3.5a. A commercial achromat doublet developed by Edmund Optics was introduced to the setup along with a spherical-aspherical lens and a curved sensor. The vignetting of the setup was modified to limit the marginal rays in order to control the sensor size. In the Appendix Fig. A.9 can be found the relative illumination of every setup where the vignetting is altered, making sure that it is not increased too much and goes below the HVS requirements (see Fig. A.9). As observed in Fig.3.5b and c. the imaging performance of the setup is quite high than the previous polychromatic setups, but still does not fulfill HVS requirements for certain areas. SAS and PTB aberrations should be also decreased (See Table 3.2) as well as the sensor size (21.4 mm).

Another customized doublet design is proposed in Fig. 3.5d. A flat sensor was placed back and a full aspherical lens, reducing the sensor size (14.93 mm), the OAL (23.67 mm) and the aberrations (SAS from -10.58 to -5.22 and PTB from -15.87 to -7.83). The imaging capabilities were improved but still, some areas are not fulfilled for the sagittal rays (See Fig. 3.5e).

3.5 Back to spherical

As observed in section 3.3, the achromat doublet has improved the imaging capabilities of the system, but still, the requirements are not fully accomplished, so another trial needs to be done. In this next step, another lens was introduced to the setup and all the aspherical surfaces were replaced by spherical ones, thus having a spherical setup. Several trials were attempted (See Fig. 3.6a to d), introducing two doublets and trying again curved and flat sensors. The best attempt is presented in Fig. 3.6e with two singlets and a doublet, where the imaging capabilities were totally satisfied (See Fig. 3.6f,g) but at the expense of high astigmatism values, Petzval blur and a large OAL (33 mm). The curvature of the sensor must be

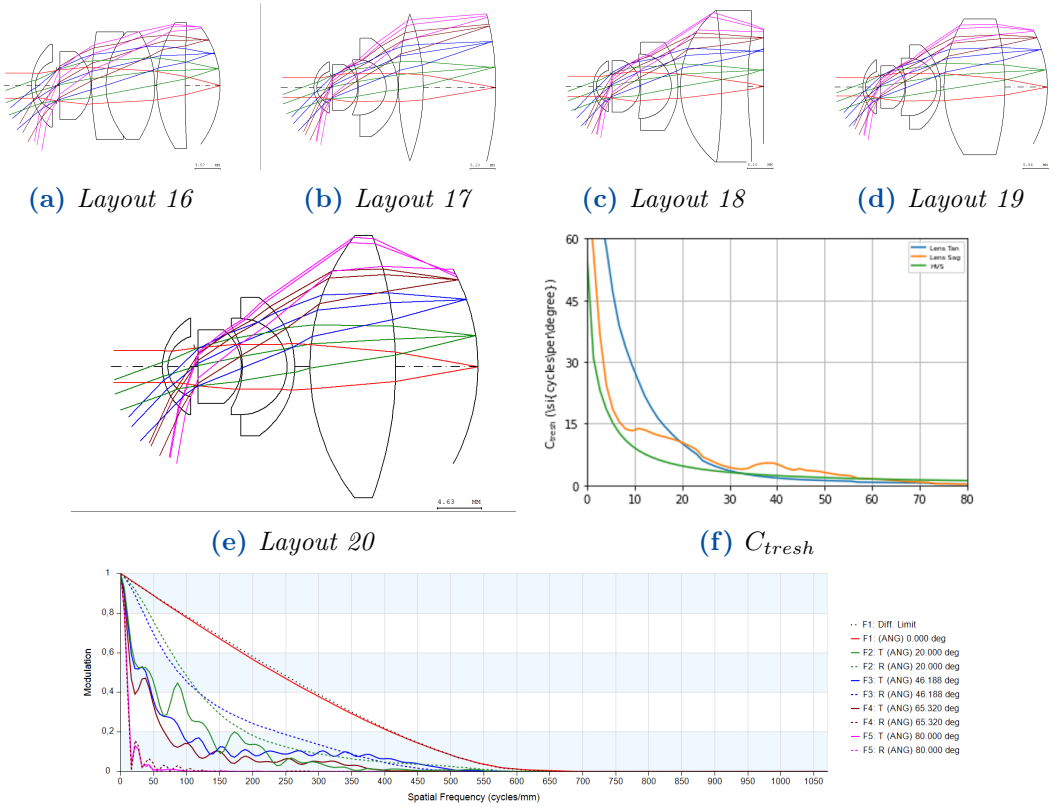

(a) *Layout 16* **(b)** *Layout 17* **(c)** *Layout 18* **(d)** *Layout 19*

(e) *Layout 20* **(f)** C_{tresh}

(g) *Optical MTF*

Figure 3.6: *Spherical designs. In (a)-(e) light propagates from left (cornea) to right (retina). In (f), C_{tresh} cycles vs degree is presented, with HVS (green line) vs Design (blue/orange line) performance. In (g) is plotted the diffractive MTF of the system (diffraction limits the best performance that can be achieved).*

decreased.

3.6 Diffractive surface

In order to fulfill again all the desired requirements, the possibility of adding a diffractive surface to the setup was explored Smith (2008), where the wavefront is altered by creating a 'grating' and modified to achieve good imaging capabilities and reduce aberrations in this specific case. Several attempts were again performed (See Fig. 3.7) where the first singlet and the doublet were finally merged into a triplet.

The final layout is presented in Fig 3.8a. A triplet and a diffractive-conic surface in the anterior face of the last lens. The aberrations are reduced again (see Design

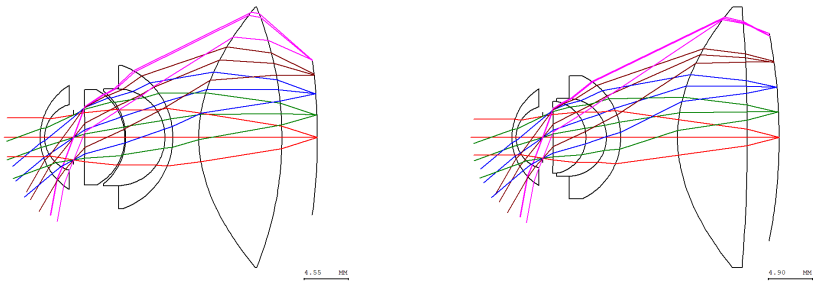

(a) *Layout 21* **(b)** *Layout 22*

Figure 3.7: *Diffractive designs. Light propagates from left (cornea) to right (retina).*

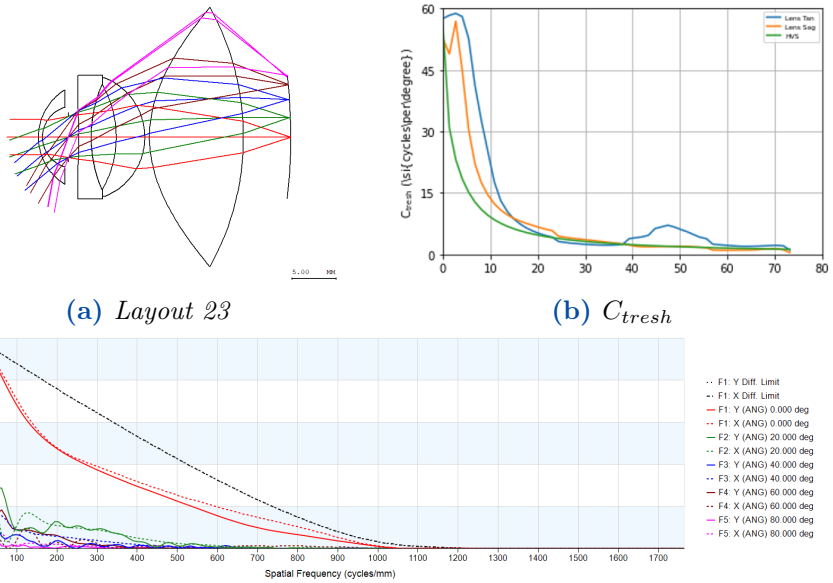

(a) *Layout 23* **(b)** C_{tresh}

(c) *Optical MTF*

Figure 3.8: *Final diffractive design. In (a) light propagates from left (cornea) to right (retina). In (b), C_{tresh} cycles vs degree is presented, with HVS (green line) vs Design (blue/orange line) performance. In (c) is plotted the diffractive MTF of the system (diffraction limits the best performance that can be achieved).*

23 in Table 3.2), as well as the OAL (28.62 mm) and the sensor size (14 mm). The relative illumination is also accomplished (Fig. A.9d) and the spot diagram seems quite reduced for almost all the different fields (See Fig.A.8g). The imaging requirements are also fulfilled, so all the required constraints are finally met for this design.

3.7 Discussion

After presenting all the different layouts, a comparison among them can be carried out. In Table 3.3, are displayed the different constraint parameters achieved for each design. The first thing to comment on is the effective focal length (EFL). As observed, the requirement for an EFL of at least 17 mm was not fulfilled for any of the designs. As commented in section 3.3, some trials were devoted to reach a larger EFL, but the rest of the constraints were not fulfilled by far when accomplishing this one (OAL, lenses and sensor size larger than 40 mm, image quality not good). It is for this reason that this constraint was not considered as the main one when designing the eye prototype, but it shall be considered for future designs, since the pixel pitch at the center of the field (given by EFL) will limit resolution for these designs. Regarding the OAL and sensor curvature, the worst results were achieved for layout 13, where it was tried to mimic the monochromatic design in polychromatic, but it did not work out. In layout 20 the image quality achieved was really good, but at the expense of a large OAL and an unrealistic curved sensor. For the rest of the designs the OAL achieved was within the established ranges, with the optimal one for the customized doublet (Design 15), since the most common axial length is around 24mm Roy et al. (2015); Bhardwaj and Rajeshbhai (2013). Regarding the sensor size, all the designs proposed are inside allowed the range for the CMOS sensor firstly proposed (CMV12000), but more work towards the reduction of the sensor size should be done, for the possible implementation of other smaller sensors (e.g., SONY IMX 541) ideally of a size up to 12.5mm. The number of surfaces was drastically reduced if compared with the reference setup (Design 1). Starting from 17 surfaces, it was reduced to 9 for the monochromatic setup (Design 8), finishing with 11 for the last diffractive setup. Lastly, the image quality threshold established for the layout in the 2nd column of Table 3.3 was achieved gradually. For the proposed monochromatic design, these requirements were successfully achieved by far, but it is true that the design is unrealistic accounting only for a monochromatic source. Then, for the first polychromatic proposal (Design 13), the requirements were not fulfilled at all in any field, improving a bit for the commercial Edmund Optics doublet achromat (Design 14) and nearly satisfying them in the customized doublet proposed in Design 15, since the tangential rays were above the HVS threshold (See Fig.3.5e). For the last two proposed designs (20, 23), it was finally fulfilled. In Design 20, again, at the expense of the other constraints as previously stated, and in Design 23 by implementing a diffractive surface, thus helping in the accomplishment of almost all the constraints.

By looking at the aberrations, (see Tables 3.2, 3.1). In the appendix is also displayed a full list of the third-order aberrations for all the presented setups (Table

Table 3.3: *Comparison of the different constraint parameters obtained for each layout. IMG refers to the imaging contrast threshold for the HVS (at least 10-25% for the center field MTF in 60 cycles/degree), OAL (starting from 22 mm and up to 30 mm), EFL to the effective focal length (17 - 20 mm), Ssize to the sensor size (< 28 mm), Scurv to the curvature of the sensor (> 3x Ssize) and N°surf to the number of surfaces (the less, the better). Here, OAL, EFL, Ssize and Scurv are expressed in millimetres. Color green indicates satisfied, whereas red means unsatisfied.*

Constraints comparison						
Design	IMG	OAL	EFL	Ssize	Scurv	N°surf
1	✓	26.57	5.43	12.56	∞	17
8	✓	27.17	7.10	17.70	-61.36	9
13	×	34.76	9.32	20.7	-34.08	9
14	×	29.85	8.30	21.2	-60	10
15	≈	23.41	6.73	14.92	∞	10
20	✓	33.17	9.53	20.38	-21.23	12
23	✓	28.62	6.38	14	-60	11

A.1)) the main ones that are high throughout all the designs are astigmatism (SAS and TAS) and the Petzval blur (PTB). Since the starting setup (see Fig. 3.1), those are the aberrations with the highest values. Note that in several setups the TAS is 0 or almost 0, since it was the higher aberration before optimization, it was always targeted to be minimized/eliminated. Regarding the rest of the aberrations, none of them interfere too much with the good development of the different setups. Spherical aberrations, Petzval curvature, axial and lateral color do not overpass ± 1 in any of the proposed designs. Slight coma values are achieved in Design 15 (1.409), but not too significant to interfere with the desired image quality. As mentioned in section 2, the large distortion values are common in this kind of design, as well as are present in the human eye and do not interfere with the required image quality.

When optimizing the different layouts, if trying to minimize different aberrations at once, either the software provides unrealistic designs and/or the image forming capabilities of the setup are drastically decreased. One example can be observed for the customized doublet (Design 15) where the aberrations were considerably reduced but the image contrast threshold was not fulfilled. A clear example in the other way around can be observed in Design 20. The imaging cutoff frequencies are met, and the MTF achieved seems fine, but the aberrations appearing in the system are considerably high. A trade-off between good image quality and minimized aberrations is needed.

Another point to tackle seeing these results is whether the sensor curvature has an important impact or not in the designs. When prototyping the different layouts,

it is true that having a curvable focal plane array (FPA) during the optimization provides interesting and good solutions that may not be achieved with a plane FPA. But if the results obtained are analyzed, the outcomes obtained for the flat vs the curved sensor are mostly the same. Even in Design 15, with the flat sensor, one of the lowest aberration values has been obtained if compared with other curved layouts. It is also true that the constraints provided by the manufacturer in order to induce this curvature are quite demanding. The sensor curvature has to be at least three times bigger than the size of it, so this limits quite a lot the different designs. Having more room to curve them, or designing a free-form sensor may increase potentially the performance of the designs, as observed for example in Design 20, where the sensor is excessively curved but the MTF obtained is quite good. Regarding the different surfaces used, the all-spherical reference Design 1 was altered in almost all the rest of the proposals. No design of the new ones has achieved the same image quality/constraints requirement as the starting one with only spherical surfaces, but it needs to be mentioned that this design is monochromatic, thus simplifying considerably the complexity of the design in order to meet criteria. With just an aspherical lens and a spherical lens, the performance of the first setup was overcome. It is true that an aspherical surface may increase the manufacturing price and complexity, but it also needs to be considered that several spherical lenses from the layout are being removed. The room for improvement regarding aberration correction of the aspherical surfaces is very noticeable when introducing them in the design if compared with only spherical surfaces. The same can be said for the conic or diffractive lens, but having a grating in the setup will also increase the price and difficult fabrication. Lastly, it has to be considered whether to have a reduced costly setup with aspherical/diffractive/conic surfaces or an all-spherical one cheaper with a higher number of surfaces.

The results obtained are acceptable and meet almost all the required criteria, but there is always room for improvement. The performance achieved by Allain and Thibault (2022) has been achieved with a simpler and reduced setup and accounting for the complete HVS FoV (160°), whereas other models account for narrower fields of view (Arianpour et al. (2013) only 34.5° and Escudero-Sanz and Navarro (1999) up to 120°). It would be ideal to simplify the setup, going back again to all spherical for a polychromatic design, minimizing cost while at the same time optimizing accuracy. The EFL should be considered for the next optimization rounds, trying to accomplish it while meeting the rest of the constraints in order to achieve an accurate center resolution. A flat sensor can be also considered back in the design, at least until manufacturing constraints are more relaxed and provide more room for testing and improvement. This way to tackle the problem, going step by step, has stated what works and what does not in the design, going step by step trying to find the exact point where the criteria are met to not overcomplicate

the setup.

3.7.1 Answering research questions

After discussing the different proposed models and reaching some final conclusions, the research questions proposed in Section 1 will be answered:

1. In an artificial eye model, how can human vision be reproduced as simply as possible, while respecting the eye's form factor and achieving good imaging resolution?

   It has been demonstrated that the number of optical surfaces can be considerably reduced by simply adding some aspherical surfaces to the setup, while still achieving good OAL, acceptable aberrations and good image quality. It is true that the complexity and possible manufacturing expense are increased if compared with an all-spherical design.

2. Is there a significant difference in the implementation of a flat sensor vs. a curved sensor in order to simulate the retina?

   While analysing the results, the outcomes obtained for the flat vs the curved sensor are mostly the same. The sensor curvature does not improve significantly the performance of the overall design since the sensor curvature that can be manufactured at the time is very restricted.

3. Which are the main problematic optical aberrations for the designs under study?

   The main aberrations that are high throughout all the proposed designs are astigmatism (SAS and TAS) and Petzval blur (PTB). It is true that in some Designs TAS is minimized since the value obtained was too high, thus the optimization process was focused to eliminate it. The rest of the aberrations do not achieve high values and they do not interfere too much with the good development of the different setups.

4 | Conclusions

In this thesis, the *'Optical Design of a Human Eye Inspired Lens'* has been proposed. The Project starts with an introduction to the eye's anatomy, neurological parts and the motivation to create these eye models, which is mainly the medical field. For better comprehension, a full review of the models proposed was carried out. Several theoretical models have been studied, where the main objective is to replicate the anatomical surfaces of the eye in a more or less restricted way. Contrast sensitivity models were also studied, where they also take into account the brain processing part of the image captured by the eye. Interesting recent models were found such as Mantiuk et al. (2022), performing an exhaustive examination of this contrast threshold mostly useful for AR/VR applications, but complete models like Barten (1999), were enough to understand and establish the constraints for our model. Once understood the different models, a balance was established between theoretical and sensitivity models. Since the main objective for the design of the eye model prototypes are the imaging capabilities, only the first surface resembling the cornea was proposed following the theoretical CAGE eye model, with an average entrance pupil size of 3.5 - 4 mm. For the rest of surfaces/components, more freedom was allowed.

The constraints to start the optical modelling of the design were also proposed (OAL, EFL, sensor size, sensor curvature, etc. See Table 2.1), and the optical simulation software CODE V was presented Synopsys, Inc. (2023) along with the pipeline followed in it to achieve potential results. It needs to be considered that this design process has been performed in gradual stages, tackling the different constraints with the main objective of achieving good image quality in the setup. The first spherical monochromatic setup (Design 1) was used as the starting/reference point. A potential monochromatic design was proposed, reducing considerably the number of surfaces of the setup and introducing an aspherical lens (Design 8). The same architecture was followed for the polychromatic setup but it did not achieve promising results (Design 13). Commercial and customized achromat doublets were tried while trying to change the approach, achieving better performance but still not good enough to meet the criteria (Designs 14, 15). The achromat approach was performed by adding another lens and using all spherical lenses

(Design 20), achieving good imaging quality but at the expense of the rest of the constraints. Lastly, another layout is proposed introducing a diffractive surface that may increase the manufacturing cost but meets the criteria (Design 23).

The main discoveries while developing the eye prototypes are the following. It has been found that astigmatism and Petzval blur are the main problematic aberrations for the design under study. The sensor curvature does not improve significantly the performance of the overall design since the sensor curvature that can be manufactured at the time is very restricted. The use of aspherical surfaces improves the results and helps considerably when reducing the number of surfaces and aberrations in the setup as well as the achromatic lens implemented in the designs (commercial Edmund Optics doublet and customized doublet/triplet). There is a trade-off between acceptable image quality and acceptable aberration values. Removing surfaces and simplifying construction is an improvement on the design using a curved surface, regardless of the similar image quality achieved.

For future work, another way to tackle EFL needs to be performed, since the results for the proposed eye models do not meet this criterium and it is of high importance to have a good image quality. This may be achieved by providing more magnification on the center field of the eye models. More detailed work on these designs may lead to better performance and results, achieving simpler layouts with better image quality and lower aberration values. It is also very important to check constantly the state of the art, for potential upgrades for example in the sensor curvature (higher curvature would be interesting), free-form surfaces or any other potential technologies arising that may be applicable in designing human eye models.

A | Appendix

Surface #	Surface Name	Surface Type	Y Radius	Thickness	Glass	Refract Mode	Y Semi-Aperture
Object		Sphere	Infinity	Infinity		Refract	
1		Sphere	6.3241	0.4608	NBK7_SCHOTT	Refract	4.9724
2		Sphere	3.5382	2.9583	AIR	Refract	3.3921
Stop		Sphere	Infinity	0.1000	AIR	Refract	1.8192
4		Sphere	Infinity	0.4442		Refract	1.9760
5		Sphere	-23.6081	0.9698	SK16_SCHOTT	Refract	1.8735
6		Sphere	-7.8396	0.6034		Refract	2.2918
7		Sphere	-4.2987	0.6716	SF58_SCHOTT	Refract	2.4718
8		Sphere	-30.1541	2.7771	LAKL12_SCHOTT	Refract	4.6034
9		Sphere	-5.7098	0.1000		Refract	4.4751
10		Sphere	-234.3908 V	3.4971	LAKL12_SCHOTT	Refract	7.2773
11		Sphere	-11.1796 V	0.1000 V		Refract	7.2773
12		Sphere	19.6609 V	3.5753	LAKL12_SCHOTT	Refract	8.9570
13		Sphere	-69.8162 V	1.2936 V		Refract	8.9306
14		Sphere	11.1329	4.9350	LAKL12_SCHOTT	Refract	8.1574
15		Sphere	-66.7477	0.7500	SF58_SCHOTT	Refract	8.2608
16		Sphere	13.8419	3.3394 V		Refract	6.6278
Image		Sphere	Infinity	0.0000		Refract	6.2884

Figure A.1: *Optical parameters for the reproduction of Lens layout 1. 16 surfaces and a flat sensor with all spherical components.*

Surface #	Surface Name	Surface Type	Y Radius	Thickness	Glass	Refract Mode	Y Semi-Aperture
Object		Sphere	Infinity	Infinity		Refract	
1		Sphere	7.7000	0.5500	NBK7_SCHOTT	Refract	5.2613
2		Sphere	3.5382	2.9583	AIR	Refract	3.3387
Stop		Sphere	Infinity	0.0000	AIR	Refract	2.1147
4		Sphere	Infinity	0.4420		Refract	2.1147
5		Asphere	-29.3102	8.1619 V	755201.275795	Refract	2.7553
6		Asphere	-6.6558	2.3081 V		Refract	6.3014
7		Sphere	33.6637 V	3.9211 V	LAKL12_SCHOTT	Refract	8.8959
8		Sphere	-40.2844 V	8.8376 V		Refract	9.0334
Image		Sphere	-61.3689 V	-0.0002		Refract	8.8545

Y Radius	-29.3102 V
Conic Constant (K)	2.7675 V
4th Order Coefficient (A)	-0.0007 V

(a) *Aspherical parameters for surface 5*

Y Radius	-6.6558 V
Conic Constant (K)	-0.2222 V
4th Order Coefficient (A)	4.3265e-05 V

(b) *Aspherical parameters for surface 6*

Figure A.2: *Optical parameters for the reproduction of lens layout 8. 8 surfaces and a curved sensor. Lens 2 (surfaces 5 and 6) is aspherical.*

Surface #	Surface Name	Surface Type	Y Radius	Thickness	Glass	Refract Mode	Y Semi-Aperture
Object		Sphere	Infinity	Infinity		Refract	
1		Sphere	7.7000	0.5500	NBK7_SCHOTT	Refract	5.2613
2		Sphere	3.5382	2.9583	AIR	Refract	3.3387
Stop		Sphere	Infinity	0.0000	AIR	Refract	2.1147
4		Sphere	Infinity	0.4420		Refract	2.3770
5		Conic	-20.8712 V	7.4615 V	508103.682459 V	Refract	2.7171
6		Conic	-5.8592 V	2.5255 V		Refract	5.9586
7		Sphere	21.0776 V	12.3781 V	620410.603236 V	Refract	11.9279
8		Sphere	-45.5605 V	8.4480 V		Refract	11.8444
Image		Sphere	-34.0807 V	0.0000		Refract	10.3509

Figure A.3: *Optical parameters for the reproduction of Lens layout 13. 8 surfaces and a curved sensor. The Conic parameter (K) for surfaces 5 and 6 are 12.96 and -0.23 respectively.*

Surface #	Surface Name	Surface Type	Y Radius	Thickness	Glass	Refract Mode	Y Semi-Aperture
Object		Sphere	Infinity	Infinity		Refract	
1		Sphere	5.9560	0.5822	NBK7_SCHOTT	Refract	4.7826
2		Sphere	3.2826	2.7500	AIR	Refract	3.1606
Stop		Sphere	Infinity	0.0000	AIR	Refract	1.9852
4		Sphere	Infinity	0.1000 V		Refract	2.2556
5		Sphere	Infinity	6.3057 V	487942.703549 V	Refract	2.0000
6		Asphere	-4.6690 V	0.1000 V		Refract	4.5000
7		Sphere	33.1500	4.0000	NSF66_SCHOTT	Refract	6.6075
8		Sphere	11.1800	12.5700	NBASF64_SCHOTT	Refract	7.7360
9	Edmund Optics 65552	Sphere	-15.1300	3.4425 V		Refract	9.9966
Image		Sphere	-60.0000	-0.0002		Refract	10.6908

Y Radius	-4.6690 V
Conic Constant (K)	-7.7104 V
4th Order Coefficient (A)	-0.0089 V
6th Order Coefficient (B)	0.0013 V
8th Order Coefficient (C)	-0.0002 V
10th Order Coefficient (D)	1.8959e-05 V
12th Order Coefficient (E)	-1.4594e-06 V
14th Order Coefficient (F)	8.0999e-08 V
16th Order Coefficient (G)	-3.0116e-09 V
18th Order Coefficient (H)	6.4829e-11 V
20th Order Coefficient (J)	-5.9445e-13 V

(a) *Aspherical parameters for surface 6*

Figure A.4: *Optical parameters for the reproduction of lens layout 14. 9 surfaces and a curved sensor. Aspherical surface in 6 and commercial triplet implemented.*

Surface #	Surface Name	Surface Type	Y Radius	Thickness	Glass	Refract Mode	Y Semi-Aperture
Object		Sphere	Infinity	Infinity		Refract	
1		Sphere	6.3241	0.4608	NBK7_SCHOTT	Refract	4.8212
2		Sphere	3.5382	2.9583	AIR	Refract	3.3291
Stop		Sphere	Infinity	0.1000	AIR	Refract	1.4911
4		Sphere	Infinity	0.4420		Refract	1.5000
5		Asphere	-6.9353 V	3.3624 V	505315.685202 V	Refract	1.8000
6		Asphere	-3.4062 V	0.1000 V		Refract	3.2000
7		Sphere	10.2441 V	5.5505 V	620410.603236 V	Refract	6.1438
8		Sphere	-8.2180 V	8.5000 V	755201.275795 V	Refract	6.1381
9		Sphere	Infinity	1.2000		Refract	6.9962
Image		Sphere	Infinity	0.0000		Refract	7.1577

Y Radius	-6.9353 V
Conic Constant (K)	2.1727 V
4th Order Coefficient (A)	-0.0051 V
6th Order Coefficient (B)	3.9037e-05 V
8th Order Coefficient (C)	-0.0001 V
10th Order Coefficient (D)	-2.3351e-05 V
12th Order Coefficient (E)	-8.7821e-06 V
14th Order Coefficient (F)	9.6632e-07 V
16th Order Coefficient (G)	1.6239e-15 V
18th Order Coefficient (H)	2.9064e-17 V
20th Order Coefficient (J)	4.5404e-19 V

(a) *Aspherical parameters for surface 5*

Y Radius	-3.4062 V
Conic Constant (K)	-0.5666 V
4th Order Coefficient (A)	-0.0016 V
6th Order Coefficient (B)	-0.0001 V
8th Order Coefficient (C)	7.3745e-05 V
10th Order Coefficient (D)	-3.0343e-05 V
12th Order Coefficient (E)	4.0584e-06 V
14th Order Coefficient (F)	-2.2157e-07 V
16th Order Coefficient (G)	6.2769e-09 V
18th Order Coefficient (H)	-6.3962e-10 V
20th Order Coefficient (J)	1.9432e-11 V

(b) *Aspherical parameters for surface 6*

Figure A.5: *Optical parameters for the reproduction of lens layout 15. 9 surfaces and a flat sensor. Lens 2 (surfaces 5 and 6) is aspherical.*

Surface #	Surface Name	Surface Type	Y Radius	Thickness	Glass	Refract Mode	Y Semi-Aperture
Object		Sphere	Infinity	Infinity		Refract	
1		Sphere	5.9560	0.5822	NBK7_SCHOTT	Refract	4.7980
2		Sphere	3.2826	2.7500	AIR	Refract	3.1664
Stop		Sphere	Infinity	0.0000	AIR	Refract	1.9369
4		Sphere	Infinity	0.4420		Refract	2.3182
5		Sphere	Infinity	4.5397 V	491227.681355 V	Refract	2.0000
6		Sphere	-4.9113 V	0.1000 V		Refract	3.5000
7		Sphere	-8.4535 V	4.7019 V	500252.690319 V	Refract	4.3000
8		Sphere	-5.0765 V	0.8000 V	755201.275795 V	Refract	5.7573
9		Sphere	-8.8632 V	1.6064 V		Refract	6.6000
10		Sphere	22.5817 V	9.0000 V	743972.448504 V	Refract	12.7000
11		Sphere	-39.7376 V	8.6555 V		Refract	12.5000
Image		Sphere	-21.2397 V	0.0000		Refract	10.1925

Figure A.6: *Optical parameters for the reproduction of Lens layout 20. 11 surfaces and a curved sensor. All spherical components*

Surface #	Surface Name	Surface Type	Y Radius	Thickness	Glass	Refract Mode	Y Semi-Aperture
Object		Sphere	Infinity	Infinity		Refract	
1		Sphere	6.3241	0.4608	NBK7_SCHOTT	Refract	4.9724
2		Sphere	3.5382	2.9583	AIR	Refract	3.3921
Stop		Sphere	Infinity	1.0722	AIR	Refract	2.3289
4		Sphere	Infinity	0.1000 V		Refract	3.0000
5		Sphere	-50.6582 V	1.3887 V	755201.275795 V	Refract	3.0257
6		Sphere	15.3103 V	2.8477 V	493408.697532 V	Refract	4.5326
7		Sphere	-11.8354 V	3.2401 V	743972.448504 V	Refract	5.5109
8		Sphere	-7.2498 V	0.5256 V		Refract	6.3772
9		Conic	14.1013 V	10.6524 V	700553.487411 V	Refract	14.1702
10		Sphere	-30.3482 V	5.3775 V		Refract	14.0928
Image		Sphere	-60.0000	0.0000		Refract	7.0000

Figure A.7: *Optical parameters for the reproduction of Lens layout 23. 10 surfaces and a curved sensor. The conic parameter (K) for surface 9 is -1.511. This surface 9 is also established as a diffractive surface.*

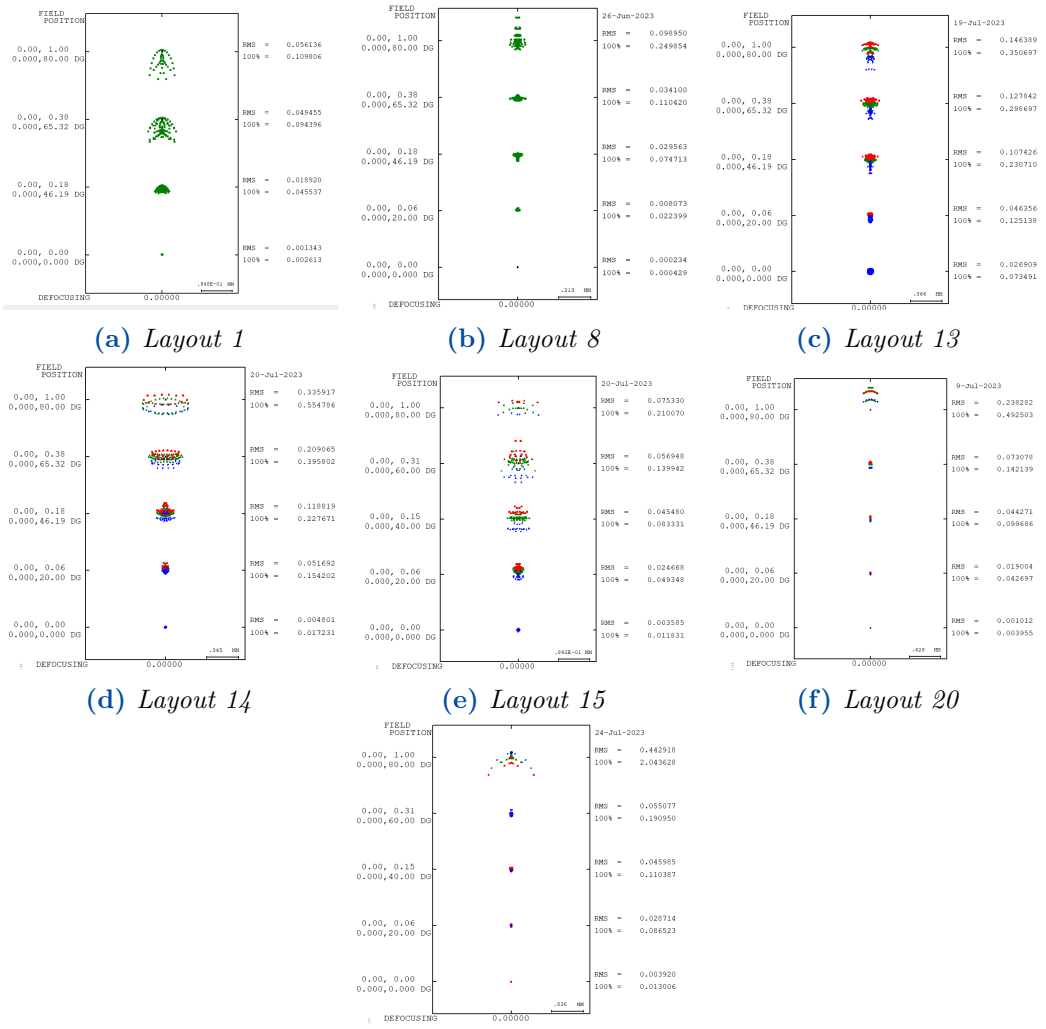

(a) *Layout 1* (b) *Layout 8* (c) *Layout 13*

(d) *Layout 14* (e) *Layout 15* (f) *Layout 20*

(g) *Layout 23*

Figure A.8: *Spot diagrams for the different proposed designs. The first image (a) consists of 4 spot sizes corresponding to 0, 46, 65 and 80 field degrees from the bottom to the top, respectively. The rest of the images consists of 5 dispersion spot diagrams, corresponding to 0, 20, 40, 60 and 80 field degrees spots from the bottom to the top, respectively. Blue color corresponds to short wavelength dispersion (426nm), green color to middle wavelength dispersion (587nm) and red color to long wavelength dispersion (656nm).*

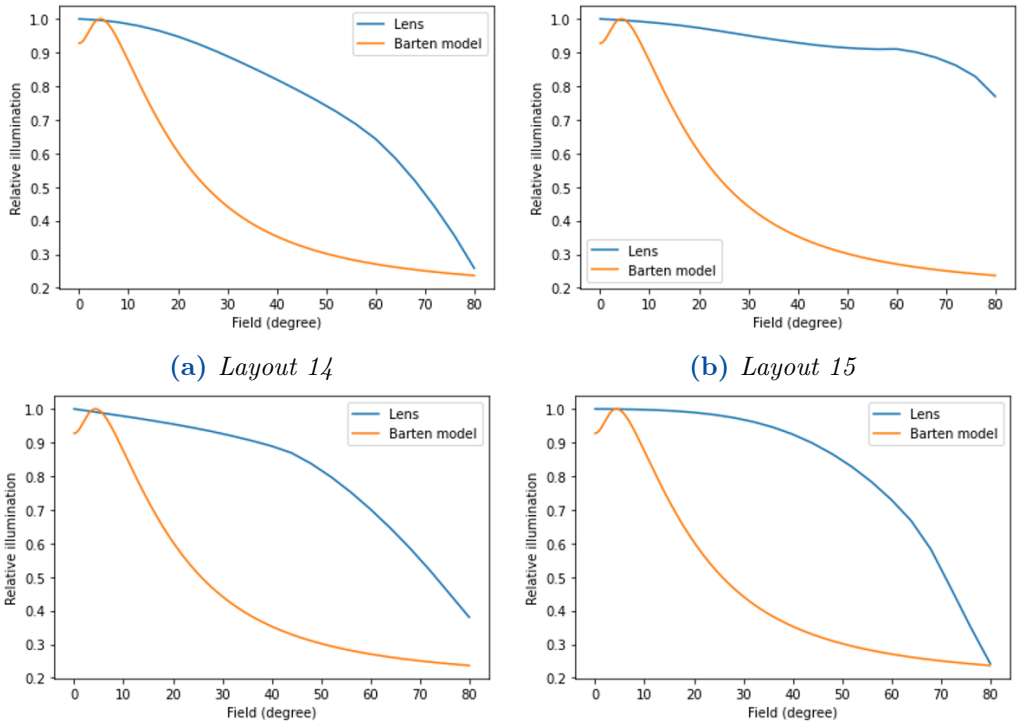

(a) *Layout 14* **(b)** *Layout 15*

(c) *Layout 20* **(d)** *Layout 23*

Figure A.9: *Relative Illumination (RI) for the different proposed designs where the vignetting is altered. The blue line represents the RI in the current design and the orange line represents the estimated RI for the HVS Barten (1999).*

Table A.1: *Full list of third order aberrations for all the presented designs. The best values (i.e., values closest to zero) for each aberration have been marked in red. Note that LAT and AX are out of the comparison for Designs 1 to 8 since there is no such aberrations on monochromatic designs.*

Third order aberrations									
Design	SA	TCO	TAS	SAS	PTB	DST	AX	LAT	PTZ
1	-0.017	0.168	-0.562	-1.558	-2.056	-458.9	0	0	-0.013
2	-0.006	0.08	-11.37	-6.255	-3.694	-559.3	0	0	-0.021
3	-0.005	-0.038	-3.062	-1.982	-1.442	-546.3	0	0	-0.008
4	-0.066	1.231	-58.94	-20.52	-1.307	-885.1	0	0	-0.003
5	-0.016	-0.027	10.99	3.982	0.479	-487.2	0	0	0.001
6	0.002	0.813	8.526	0.923	-2.878	-409.9	0	0	-0.014
7	-0.009	-0.395	0	0	0	-546.0	0	0	0
8	0.004	-0.017	-1.544	-3.172	-3.986	-470.3	0	0	-0.019
9	-0.036	1.170	-9.129	-10.75	-11.56	-419.2	-0.030	-0.510	-0.073
10	-0.058	1.307	15.83	-0.284	-8.344	-282.1	-0.088	-1.021	-0.058
11	0.003	1.452	6.316	-3.947	-9.078	-443.6	-0.034	-0.627	-0.047
12	-0.037	1.058	-25.47	-14.04	-8.325	-709.9	-0.044	-0.750	-0.035
13	-0.032	-0.277	-7.798	-5.378	-4.168	-683.3	-0.049	-0.942	-0.015
14	-0.166	-0.796	0	-10.58	-15.87	-526.8	-0.003	-0.627	-0.059
15	-0.008	1.409	0	-5.222	-7.834	-511.7	-0.005	-0.429	-0.036
16	-0.040	0.394	-15.07	-12.59	-11.35	-537.4	-0.013	-0.533	-0.058
17	-0.009	-0.379	-9.145	-10.36	-10.97	-826.7	0.002	-0.564	-0.028
18	-0.028	-0.101	-7.857	-10.27	-11.49	-767.5	0.001	-0.427	-0.036
19	-0.007	0.110	-14.70	-11.46	-9.845	-851.3	0.001	-0.593	-0.027
20	-0.008	-0.253	-15.54	-13.38	-12.30	-763.5	0	-0.551	-0.040
21	-0.011	0.301	0	-7.914	-11.07	-503.5	-0.034	-0.735	-0.055
22	-0.016	0.330	0	-7.477	-11.21	-565.4	-0.030	-0.793	-0.042
23	-0.007	0.755	0	-5.301	-7.952	-504.6	-0.041	-0.915	-0.038

Bibliography

Aguirre, G. K. (2019). A model of the entrance pupil of the human eye. *Scientific reports*, 9(1):9360. (cited on page 29)

Ahmed, S. N. (2007). *Physics and engineering of radiation detection*. Academic Press. (cited on page 4)

Al-Ahdali, I. H. and El-Messiery, M. (1995). Examination of the effect of the fibrous structure of a lens on the optical characteristics of the human eye: a computer-simulated model. *Applied optics*, 34(25):5738–5745. (cited on page 9)

Allain, G. and Thibault, S. (2022). Optical design process of a human eye inspired lens. In *Current Developments in Lens Design and Optical Engineering XXIII*, volume 12217, pages 149–154. SPIE. (cited on pages 1, 29, 32, 33, 35, 36, 47, and 68)

Amorim, A. R., Bret, B., and González-Méijome, J. M. (2022). Opto-mechanical eye models, a review on human vision applications and perspectives for use in industry. *Sensors*, 22(19):7686. (cited on page 14)

Arianpour, A., Tremblay, E. J., Stamenov, I., Ford, J. E., Schanzlin, D. J., and Lo, Y. (2013). An optomechanical model eye for ophthalmological refractive studies. *Journal of refractive surgery*, 29(2):126–132. (cited on pages 16, 17, 18, 47, and 68)

Artal, P. and Tabernero, J. (2010). Optics of human eye: 400 years of exploration from galileo's time. *Applied optics*, 49(16):D123–D130. (cited on page 8)

Atchison, D. A. (2023). *Optics of the human eye*. CRC Press. (cited on pages 5, 6, 8, 22, 25, 67, and 68)

Atchison, D. A., Markwell, E. L., Kasthurirangan, S., Pope, J. M., Smith, G., and Swann, P. G. (2008). Age-related changes in optical and biometric characteristics of emmetropic eyes. *Journal of vision*, 8(4):29–29. (cited on page 1)

Atchison, D. A. and Thibos, L. N. (2016). Optical models of the human eye. *Clinical and Experimental Optometry*, 99(2):99–106. (cited on pages 8, 10, 11, and 67)

Bakaraju, R. C., Ehrmann, K., Falk, D., Ho, A., and Papas, E. (2010). Physical human model eye and methods of its use to analyse optical performance of soft contact lenses. *Optics Express*, 18(16):16868–16882. (cited on pages 20 and 21)

Barten, P. G. (1999). *Contrast sensitivity of the human eye and its effects on image quality*. SPIE press. (cited on pages 12, 13, 14, 33, 49, 57, 67, and 70)

Bhardwaj, V. and Rajeshbhai, G. P. (2013). Axial length, anterior chamber depth-a study in different age groups and refractive errors. *Journal of clinical and diagnostic research.*, 7(10):2211. (cited on pages 23 and 45)

Bozorgian, A., Pedersen, M., and Thomas, J.-B. (2022). Modification and evaluation of the peripheral contrast sensitivity function models. *Journal of the Optical Society of America A*, 39(9):1650–1658. (cited on page 13)

Campbell, C. E. (2008). Wavefront measurements of diffractive and refractive multifocal intraocular lenses in an artificial eye. *Journal of Refractive Surgery*, 24(3):308. (cited on pages 16, 17, and 68)

Carson, D., Hill, W. E., Hong, X., and Karakelle, M. (2014). Optical bench performance of acrysof® iq restor®, at lisa® tri, and finevision® intraocular lenses. *Clinical Ophthalmology*, pages 2105–2113. (cited on page 16)

Charman, W. N. and Radhakrishnan, H. (2009). Accommodation, pupil diameter and myopia. *Ophthalmic and Physiological Optics*, 29(1):72–79. (cited on page 5)

Choi, C., Choi, M. K., Liu, S., Kim, M., Park, O. K., Im, C., Kim, J., Qin, X., Lee, G. J., Cho, K. W., et al. (2017). Human eye-inspired soft optoelectronic device using high-density mos2-graphene curved image sensor array. *Nature communications*, 8(1):1664. (cited on page 19)

CIE (1931). Commission internationale de l'eclairage proceedings. (cited on page 12)

Cook, C. A., Koretz, J. F., Pfahnl, A., Hyun, J., and Kaufman, P. L. (1994). Aging of the human crystalline lens and anterior segment. *Vision research*, 34(22):2945–2954. (cited on page 6)

Curatu, E. O., Pettit, G. H., and Campin, J. A. (2002). Customized schematic eye model for refraction correction design based on ocular wavefront and corneal topography measurements. In *Ophthalmic Technologies XII*, volume 4611, pages 165–175. SPIE. (cited on page 1)

Daly, S. J. (1992). Visible differences predictor: an algorithm for the assessment of image fidelity. In *Human Vision, Visual Processing, and Digital Display III*, volume 1666, pages 2–15. SPIE. (cited on page 12)

Dartt, D. A. (2010). *Encyclopedia of the Eye*, volume 1. Academic Press. (cited on pages 2, 6, 8, and 67)

de Castro, A., Rosales, P., and Marcos, S. (2007). Tilt and decentration of intraocular lenses in vivo from purkinje and scheimpflug imaging: validation study. *Journal of Cataract & Refractive Surgery*, 33(3):418–429. (cited on page 15)

Eglen, S. J. (2012). Cellular spacing: Analysis and modelling of retinal mosaics. *Computational Systems Neurobiology*, pages 365–385. (cited on page 7)

Emsley, H. H. (1936). *Visual optics*. Hatton Press, London. (cited on pages 9, 10, and 11)

Escudero-Sanz, I. and Navarro, R. (1999). Off-axis aberrations of a wide-angle schematic eye model. *Journal of the Optical Society of America A*, 16(8):1881–1891. (cited on pages 10, 17, and 47)

Esteve-Taboada, J. J., Del Águila-Carrasco, A. J., Marín-Franch, I., Bernal-Molina, P., Montés-Micó, R., and López-Gil, N. (2015). Opto-mechanical artificial eye with accommodative ability. *Optics express*, 23(15):19396–19404. (cited on page 16)

Fedtke, C., Manns, F., and Ho, A. (2010). The entrance pupil of the human eye: a three-dimensional model as a function of viewing angle. *Optics express*, 18(21):22364–22376. (cited on page 29)

Gao, W., Xu, Z., Han, X., and Pan, C. (2022). Recent advances in curved image sensor arrays for bioinspired vision system. *Nano Today*, 42:101366. (cited on page 19)

Gliddon, G. H. (1929). An optical replica of the human eye for the study of the retinal image. *Archives of Ophthalmology*, 2(2):138–163. (cited on page 17)

Gobbi, P. G. (2012). Modeling the optical and visual performance of the human eye. In *Modeling the optical and visual performance of the human eye*. SPIE. (cited on pages 1, 10, and 12)

Gobbi, P. G., Carones, F., and Brancato, R. (1999). Optical eye model for photorefractive surgery evaluation. In *Ophthalmic Technologies IX*, volume 3591, pages 10–21. SPIE. (cited on page 1)

Greivenkamp, J. E., Schwiegerling, J., Miller, J. M., and Mellinger, M. D. (1995). Visual acuity modeling using optical raytracing of schematic eyes. *American journal of ophthalmology*, 120(2):227–240. (cited on pages 9 and 10)

Gu, L., Poddar, S., Lin, Y., Long, Z., Zhang, D., Zhang, Q., Shu, L., Qiu, X., Kam, M., Javey, A., et al. (2020). A biomimetic eye with a hemispherical perovskite nanowire array retina. *Nature*, 581(7808):278–282. (cited on pages 19 and 68)

Guenter, B., Joshi, N., Stoakley, R., Keefe, A., Geary, K., Freeman, R., Hundley, J., Patterson, P., Hammon, D., Herrera, G., et al. (2017). Highly curved image sensors: a practical approach for improved optical performance. *Optics express*, 25(12):13010–13023. (cited on page 19)

Gullstrand, A. (1909). Helmholtz handbuch der physiologischen optik (jp southall, trans.). *Optical Society of America, USA*, 301. (cited on pages 6, 8, 9, and 11)

Hautière, N., Tarel, J.-P., and Brémond, R. (2007). Perceptual hysteresis thresholding: Towards driver visibility descriptors. In *2007 IEEE International Conference on Intelligent Computer Communication and Processing*, pages 89–96. IEEE. (cited on pages 3 and 67)

Hitzenberger, C. K. (1991). Optical measurement of the axial eye length by laser doppler interferometry. *Investigative ophthalmology & visual science*, 32(3):616–624. (cited on page 23)

Hou, F., Lu, Z.-L., Bex, P., and Reynaud, A. (2021). The contrast sensitivity function: From laboratory to clinic. (cited on page 2)

Hugot, E., Lombardo, S., Behaghel, T., Chambion, B., Jahn, W., Gaschet, C., Hugot, S., Gach, J. L., Ferrari, M., and Henry, D. (2019). Curved sensors: experimental performance of cmos prototypes and wide field related imagers. In *International Conference on Space Optics—ICSO 2018*, volume 11180, pages 1127–1133. SPIE. (cited on page 19)

Imatest (2023). Mtf measurement consistency. `https://www.imatest.com/support/docs/pre-5-2/mtf-measurement-consistency/`. Accessed: 05/08/2023. (cited on page 4)

Jaeger, W. (1986). Johannes kepler's contributions to ophthalmologic optics. *Klinische Monatsblatter fur Augenheilkunde*, 188(2):163–166. (cited on page 8)

Kim, M., Lee, G. J., Choi, C., Kim, M. S., Lee, M., Liu, S., Cho, K. W., Kim, H. M., Cho, H., Choi, M. K., et al. (2020). An aquatic-vision-inspired camera based on a monocentric lens and a silicon nanorod photodiode array. *Nature Electronics*, 3(9):546–553. (cited on page 19)

Kim, M. S., Kim, M. S., Lee, G. J., Sunwoo, S.-H., Chang, S., Song, Y. M., and Kim, D.-H. (2022). Bio-inspired artificial vision and neuromorphic image processing devices. *Advanced Materials Technologies*, 7(2):2100144. (cited on page 19)

Ko, H. C., Stoykovich, M. P., Song, J., Malyarchuk, V., Choi, W. M., Yu, C.-J., Geddes Iii, J. B., Xiao, J., Wang, S., Huang, Y., et al. (2008). A hemispherical electronic eye camera based on compressible silicon optoelectronics. *Nature*, 454(7205):748–753. (cited on page 19)

Kooijman, A. C. (1983). Light distribution on the retina of a wide-angle theoretical eye. *Journal of the Optical Society of America A*, 73(11):1544–1550. (cited on page 9)

Liang, D., Xiang, K., Du, J.-W., Yang, J.-N., and Wang, X.-Y. (2014). Biomimetic optical system using polymer lenses with tunable focus. *Optical Engineering*, 53(10):105101–105101. (cited on page 18)

Liou, H.-L. and Brennan, N. A. (1997). Anatomically accurate, finite model eye for optical modeling. *Journal of the Optical Society of America A*, 14(8):1684–1695. (cited on pages 9, 10, and 12)

Liu, H., Huang, Y., and Jiang, H. (2016). Artificial eye for scotopic vision with bioinspired all-optical photosensitivity enhancer. *Proceedings of the National Academy of Sciences*, 113(15):3982–3985. (cited on page 19)

Liu, Y.-J., Wang, Z.-Q., Song, L.-P., and Mu, G.-G. (2005). An anatomically accurate eye model with a shell-structure lens. *Optik*, 116(6):241–246. (cited on page 9)

Mantiuk, R. K., Ashraf, M., and Chapiro, A. (2022). stelacsf: a unified model of contrast sensitivity as the function of spatio-temporal frequency, eccentricity, luminance and area. *ACM Transactions on Graphics (TOG)*, 41(4):1–16. (cited on pages 13 and 49)

Masajada, A. P. (1999). Numerical study of the influence of the shell structure of the crystalline lens on the refractive properties of the human eye. *Ophthalmic and Physiological Optics*, 19(1):41–49. (cited on page 9)

Movshon, J. A. and Kiorpes, L. (1988). Analysis of the development of spatial contrast sensitivity in monkey and human infants. *Journal of the Optical Society of America A*, 5(12):2166–2172. (cited on page 12)

Norrby, S., Piers, P., Campbell, C., and van der Mooren, M. (2007). Model eyes for evaluation of intraocular lenses. *Applied optics*, 46(26):6595–6605. (cited on page 1)

OpenAI (2021). Chatgpt: Language generation for conversations. `https://openai.com/research/chatgpt`. (cited on page 2)

Petsch, S., Schuhladen, S., Dreesen, L., and Zappe, H. (2016). The engineered eyeball, a tunable imaging system using soft-matter micro-optics. *Light: Science & Applications*, 5(7):e16068–e16068. (cited on pages 18 and 22)

Pomerantzeff, O. (1971). Wide angle optical model of the human eye. *Annals of ophthalmology*, 3(8):815–819. (cited on page 9)

Prieto, P. M., Vargas-Martın, F., Goelz, S., and Artal, P. (2000). Analysis of the performance of the hartmann–shack sensor in the human eye. *Journal of the Optical Society of America A*, 17(8):1388–1398. (cited on page 16)

Rim, S.-B., Catrysse, P. B., Dinyari, R., Huang, K., and Peumans, P. (2008). The optical advantages of curved focal plane arrays. *Optics Express*, 16(7):4965–4971. (cited on page 19)

Roka, A., Galambos, P., and Baranyi, P. (2009). Contrast sensitivity model of the human eye. In *2009 4th International Symposium on Computational Intelligence and Intelligent Informatics*, pages 93–99. IEEE. (cited on pages 2, 13, 14, and 67)

Rosales, P., Dubbelman, M., Marcos, S., and Van der Heijde, R. (2006). Crystalline lens radii of curvature from purkinje and scheimpflug imaging. *Journal of Vision*, 6(10):5–5. (cited on pages 15 and 68)

Rovamo, J., Luntinen, O., and Näsänen, R. (1993). Modelling the dependence of contrast sensitivity on grating area and spatial frequency. *Vision Research*, 33(18):2773–2788. (cited on pages 12 and 13)

Roy, A., Kar, M., Mandal, D., Ray, R. S., and Kar, C. (2015). Variation of axial ocular dimensions with age, sex, height, bmi-and their relation to refractive status. *Journal of clinical and diagnostic research.*, 9(1):AC01. (cited on pages 23 and 45)

Schott (2023). Schott. `https://www.schott.com/en-gb/interactive-abbe-diagram`. Accessed: 05/06/2023. (cited on pages 31 and 68)

Smith, W. J. (2008). *Modern optical engineering: the design of optical systems*. McGraw-Hill Education. (cited on pages 32 and 43)

Staugaard, C. F., Petersen, A., and Vangkilde, S. (2016). Eccentricity effects in vision and attention. *Neuropsychologia*, 92:69–78. (cited on page 7)

Synopsys, Inc. (2023). Code V. `https://www.synopsys.com/optical-solutions/codev.html`. Version 12.3. (cited on pages 2, 4, 23, 24, 49, 67, and 68)

Thibos, L. N., Ye, M., Zhang, X., and Bradley, A. (1992). The chromatic eye: a new reduced-eye model of ocular chromatic aberration in humans. *Applied optics*, 31(19):3594–3600. (cited on pages 9 and 10)

Thomas, C. W., Gilmore, G. C., and Royer, F. L. (1993). Models of contrast sensitivity in human vision. *IEEE transactions on systems, man, and cybernetics*, 23(3):857–864. (cited on page 12)

Westland, S., Owens, H., Cheung, V., and Paterson-Stephens, I. (2006). Model of luminance contrast-sensitivity function for application to image assessment. *Color Research Application*, 31:315 – 319. (cited on page 12)

BIBLIOGRAPHY

List of Figures

List of Tables